Complex muscle architecture described with diffusion weighted MRI

by

Terry A. Gaige

Submitted to the Department of Mechanical Engineering
in partial fulfillment of the requirements for the degree of

Master of Science in Mechanical Engineering

at the

MASSACHUSETTS INSTITUTE OF TECHNOLOGY

June 2007

Author . . . .
Department of Mechanical Engineering
May 18, 2007

Certified by . . . .
Roger Kamm
ıgineering
upervisor

Certified by . . . .
ᴦᴵᴄᴴᴀᴿᴅ Gilbert
Research Scientist, Mechanical Engineering
Thᴏˢᶦˢ Supervisor

Accepted by . . . .
Lallit Anand
Chairman, Department Committee on Graduate Students

Complex muscle architecture described with diffusion weighted MRI

by

Terry A. Gaige

Abstract

The complex array of fiber orientations exhibited by muscles such as the tongue, esophagus, and heart, enable function beyond basic pulling. Among other things, the presence of crossing geometry adds the ability to push by bi-directional contraction causing expansion in the orthogonal direction. Diffusion weighted magnetic resonance imaging (DW-MRI), provides a convenient, non-destructive, method for deriving fiber architecture in many tissues. DW-MRI finely probes tissue microstructure by determining direction-specific variations of signal attenuation. Gradients are applied in a set of directions, intensities, and durations and the attenuation data combined to form an approximation of fiber alignment within each voxel. The main original contributions of this work are the calibration and application of diffusion weighted imaging methods to several muscular tissues and analysis of the data. Of particular note are: (1) the relation of diffusion spectrum MRI derived muscle architecture to 3D whole tissue two-photon microscopy data, and (2) the ability to capture mechanically relevant tongue muscle architecture data from human in vivo and analysis. Muscular tissue is involved in nearly all vital functions of biological organisms: respiration, ingestion, digestion, circulation in addition to basic motion. The application of DW-MRI technologies to muscle tissue as described in this paper could lead to insights about or aid in the remediation of muscular dystrophies and other myopathies.

Thesis Supervisor: Roger Kamm
Title: Professor, Mechanical Engineering

Thesis Supervisor: Richard Gilbert
Title: Research Scientist, Mechanical Engineering

Acknowledgments

In this section I will attempt to acknowledge all those who have contributed in their own way to completion of this research. First and most importantly, I thank Richard Gilbert, the driving force behind all of this work, for his continual mentoring and for insisting on calling me "Professor". And second, Sam Felton, my fellow graduate researcher and good friend, for keeping me sane. I thank Prof. Roger Kamm for excellent bioengineering classes, for his advice on this thesis, for a lab to call home and a desk to work on. I thank our collaborators at Massachusetts General Hospital: George Dai, Thomas Benner, Ruopeng Wang, and Van Wedeen, as well as Jon Glickman from Brigham Women's Hospital, for their expertise and willingness to share it. I thank our undergraduate student researchers, Sean Nabar, Tristan Lang, Teresa Wang and Chris Cabral for their unique perspectives and hard work. I thank Hyuk-Sang Kwon for acquiring terabytes of data on mouse tongues and especially Yoon-Sung Nam for dependably providing an endless supply of them. I thank my labmates and friends for their assistance and welcome diversions: Nate Hammond, Vernella Vickerman, Cherry Wan, Johanna Varner, Aida Abdul Rahim, Anusuya Das, Jeff Hsu, Charlene Chuang, Sungyon Lee, Barry Kudrowitz, Chester Tse, Kim Huestis, Kynam Doan, Arthur Mak, Angela Chen, Allison Kao, Jenny French, Melissa Read, and Brady Young. Thanks also to all my brothers at Chi Phi for letting me be their resident advisor the past year. I thank my friends in the San Francisco area where I spent each summer: Maria Tonione, Janet Fang, Kim Tsao, Dave Smith, Max Planck, and Philip Lee for providing me a life plan for at least the next few years. Finally, I thank my parents, Karen and David, my big sister, Dana, and little sister, Jacy, for everything else.

Contents

List of Figures

9

List of Tables

Chapter 1

Introduction

1.1 Motivation

Muscular tissue is involved in nearly all vital functions of biological organisms: respiration, ingestion, digestion, circulation in addition to basic motion. The majority of muscle in the human body is composed of myocytes aligned generally in one direction and attached at both ends to the skeleton through a tendon. Much research has been done regarding activation, strain rate and force output for these muscle types [36, 86] but the incorporation of that understanding to muscles exhibiting multi-directional fiber alignment, such as the tongue, esophagus, and heart, is less explored. Muscles with crossing fibers do not function simply by pulling. The presence of crossing geometry adds the ability to push by bi-directional contraction causing expansion in the orthogonal direction. Muscles that use this phenomenon, which is based on the near incompressibility of water, are called muscular hydrostats; of which, the mammalian tongue, the elephant trunk, and octopus tentacles are all quintessential examples. The esophagus and heart are not typically considered muscular hydrostats, but they do have complex architectures and the same principles are relevant.

Several possible methods exist and have been attempted to evaluate muscle structure, such as histological sectioning of whole tissue [77], electron microscopy with or without chemical-maceration [44, 65], or by careful dissection [54]. Histology, an inherently 2D approach is ambiguous for those fibers oriented at an angle through

the image plane, electron microscopy is limited to surface imaging of small regions, and direct dissection is tedious; additionally, all are destructive of the tissue. Figure 1.1.1 shows a histological section of a bovine esophageal wall. In this small region the muscle cells are aligned in many directions.

Figure 1.1.1: Histology of the esophageal muscularis showing the complexity of fiber alignment. Notice the ineptitude of 2D histological images at providing useful information regarding 3D architecture

A unique application of magnetic resonance imaging allows sensitivity to the direction and magnitude of water diffusion. From the assumption that water diffuses most easily parallel to barriers, this imaging technology offers a convenient, non-destructive, method for deriving fiber architecture at an intermediate multicellular scale, or *meso*scale, in many tissues. The use of these diffusion weighted magnetic resonance imaging (DW-MRI) technologies to muscle tissue as described in this paper, could lead to insights about muscular dystrophies and other myopathies. Relating tissue scale architecture to the stress and strain fields will lead to better understanding and organ morphogenesis; such as the effect of missing adhesion proteins on the development of normal cardaic architecture, or studying the structural remodeling of

tissue following infarction. Improving the methods to the point that accurate and fast fiber orientation data is achievable in vivo may also assist during image guided surgery.

1.2 Summary

In this thesis there will be a section covering the background of diffusion MRI, a section relating diffusion MRI to microstructure obtained with two-photon microscopy, and a section on each of three organs exhibiting complex myoarchitecture: tongue, esophagus, and heart.

The main original contributions of this work are the calibration and application of diffusion weighted imaging methods to various muscular tissues and analysis of the data. Of particular note are:

- the ability to capture mechanically relevant tongue muscle architecture data from human *in vivo* and analysis.

- the relation of diffusion spectrum MRI derived muscle architecture to 3D whole tissue two-photon microscopy data.

Chapter 2

Introduction to diffusion MRI

Magnetic resonance imaging (MRI) works by placing a sample in a strong magnetic field, applying a radio frequency (RF) signal which is stored in the spins of nuclei and then re-emitted. The signal response is then captured with an antenna and information about the sample reconstructed. MRI has many advantages over other imaging technologies. It is non-invasive and able to image in deep tissue with high contrast between tissue types. Resolutions range from $10 \, \mu m$ to $10 \, mm$. To present knowledge there are no secondary harmful effects other than interference with implanted devices and the innate dangers of strong magnetic fields combined with large or sharp metallic objects. Also many clever adaptations are possible, such as diffusion imaging and strain rate imaging. This chapter introduces the basic theory of magnetic resonance imaging (MRI) and provides a semi-thorough explanation of how MRI can be sensitized to the amount and direction of self-diffusion in biological tissue.

2.1 Basics of MRI

The discovery of nuclear magnetic resonance has allowed the rapid development of a very useful and widely applicable imaging technology. In 1946, Bloch [5] and Purcell [59] discovered separately that atomic nuclei with unpaired protons precess in strong magnetic fields with a frequency relative to the field strength. Most elements have at least one isotope with unpaired protons, but those most useful for MRI are

^{31}P, ^{23}Na, ^{14}N, ^{13}C, ^{19}F and, most importantly, due to its abundance in biological tissue, ^{1}H. The magnetic resonance phenomenon was initially used simply to study chemical structures, but in the early 1970's the ability to derive spatial information by introducing gradients was discovered [38, 43], thus bringing MRI into the diverse realm of medical imaging applications.

2.1.1 Magnetism and spin

The magnetic forces we are familiar with, such as those which hold esteemed artwork to the refrigerator door, originate from *electron* spin and motion. Nuclear magnetic moments, the forces originating from *proton* spin, are much weaker, but because they precess around stationary magnetic fields at a much lower frequency, a unique signal is discernible, given that enough unpaired spins are present in an imaging volume (called a voxel).

In a steady state, the net magnetization vector for a group of spins, $\mathbf{M}$, aligns itself with an external magnetic field, $\mathbf{B_0}$. If $\mathbf{M}$ is disturbed, it will precess around $\mathbf{B_o}$ at the Larmor frequency, $\omega_0 = \gamma \mathbf{B_0}$, where γ is the gyromagnetic ratio specific to each kind of nuclei. $\mathbf{M}$ can be tilted away from $\mathbf{B_0}$ by applying a perpendicular magnetic field, but since $\mathbf{M}$ rotates, this second magnetic field must rotate at the same rate to always remain perpendicular, which is done simply by applying an RF pulse, perpendicular to $\mathbf{B_0}$ and oscillating at ω_0.

If the RF pulse is stopped just as $\mathbf{M}$ has tilted 90°, $\mathbf{M}$ will slowly relax to the parallel state. As the net magnetization vector relaxes, it will continue to precess around $\mathbf{B_0}$ thereby causing a rotating magnetic field, also known as an RF signal. This signal can be sensed using an antenna or coil placed around or adjacent to the sample being imaged.

2.1.2 Image formation

In a uniform magnetic field all spins of the same material precess at the same frequency. The only information that could be received by an antenna would be the

relative portions of various materials. In order to extract spatial information about a sample, a gradient can be added on top of $\mathbf{B_0}$ which causes some spins to precess faster, and some slower, based on their location within the gradient. The most common way to identify a point in space is to first select a slice of spins by applying an RF pulse of a particular frequency while the sample is within a gradient, G_z. Gradients in the x and y-axis are then applied to establish position in the transverse xy-plane. One way is to apply a gradient, G_y, for a short period of time, which introduces a linear phase shift along y and then read the signal while a third gradient, G_x is applied, which encodes along the x-axis by frequency. These gradients are conventionally called the slice, phase, and frequency (or read), encoding gradients.

2.2 Diffusion weighted imaging

The different diffusion imaging techniques use the same principle: that signal strength decreases as a result of the random motion of water molecules within a magnetic gradient. An image is sensitized to the amount of self diffusion in a particular direction by sustaining and reversing a gradient in that direction. The protons that diffuse parallel to the gradient direction experience a dephasing that contributes to a net signal attenuation. Protons that diffuse perpendicular to the gradient direction are unaffected.

A standard diffusion weighted pulse sequence is shown in Figure 2.2.1 along with an accompanying simulation of how the spins respond in Figure 2.2.2. The simulation is shown in the rotating reference frame so the spins appear stationary in each image. First, the spins are tipped by a $\pi/2$ pulse, then they experience a steady gradient of duration δ. During this gradient the spins in the stronger field aquire more phase shift than the others. Then the spins are allowed to diffuse meanwhile being flipped a full π. Time Δ later, the gradient is reapplied and the spins regain coherence. At time of acquisition, the spins realign, creating a strong echo that is diminished by the dephasing that occurred by particles that changed position between the first and second gradient.
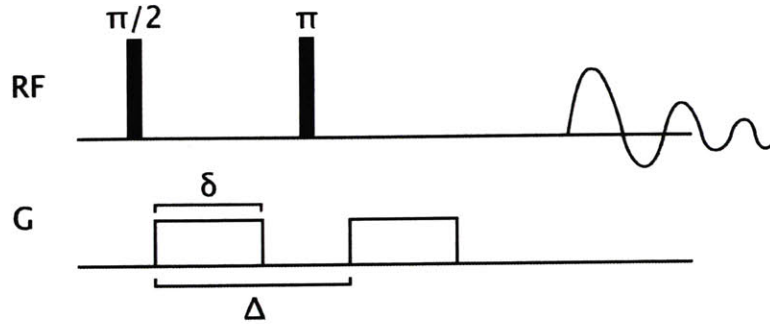
Figure 2.2.1: A typical diffusion weighted pulse sequence [33] is a modified spin-echo pulse sequence that sensitive to the attenuating effects of diffusion. The pulse sequence involves a $\pi/2$ pulse, and two gradients of duration δ seperated by Δ and a full π pulse. Readout is accomplished using typical single shot echo-planar spatial encoding.
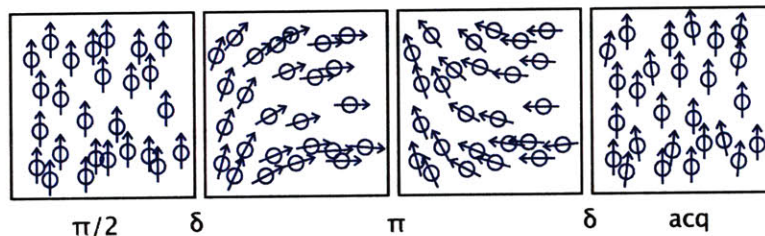
Figure 2.2.2: Simulation of a diffusion weighted MRI experiment [33]. Spins acquire a phase difference, then regain coherence diminished relative to the amount of diffusion parallel to an applied diffusion weighting gradient.

Diffusion weighted MRI can be used to finely probe tissue microstructure by determining direction-specific variations of MR signal attenuation [4]. Tissues with anisotropic fiber architectures exhibit analogous anisotropic diffusion behavior because microscopic barriers, such as cytoskeletal elements, and membranes restrict typical Brownian motion to certain preferential directions [8]. In diffusion MR imaging, gradients are applied in a set of directions, intensities, and durations and the attenuation data combined to form an approximation of fiber alignment within the voxel. The different diffusion imaging techniques: diffusion tensor, diffusion spectrum, q-ball and others, vary in how the gradients are applied and how they reconstruct the resulting approximation of diffusion.

2.2.1 Diffusion Tensor Imaging

The diffusion tensor model depicts the net diffusion in a volume of tissue with a symmetric second rank tensor. The diffusion tensor can be interpreted physically as an ellipsoid with its axes constructed along its three orthogonal eigenvectors and with each axis length proportional to the appropriate eigenvalues. The longest axis, i.e. direction of greatest diffusion, is assumed to correlate to local muscle fiber orientation. The extent of signal attenuation relates to the applied gradient and the diffusion tensor according to:

$$\ln \frac{S_b}{S_o} = -b\vec{q_i}^T \boldsymbol{D} \vec{q_i} \qquad (2.2.1)$$

where S_b is the signal of the attenuated image at each voxel, S_o is from the unattenuated image, $\boldsymbol{D}$ is the diffusion tensor, and b is the scalar quantity termed the b value, which is a function of the shape, temporal spacing, duration and magnitude of the diffusion weighting gradient pulses. The vector $\vec{q_i}$ is a unit vector in the direction of the ith applied gradient. The six unique coefficients of the diffusion tensor, $\boldsymbol{D}$, can be found by applying a minimum of 6 non-collinear diffusion-weighting gradients and comparing the resulting images to one unattenuated image. To improve signal to noise, gradients are applied in numerous evenly spaced directions arrayed on the surface of a sphere, resulting in a system of linear equations that over-constrains the components of the diffusion tensor and may be solved using multiple linear regression.

Though useful, the tensor model chooses only a single diffusion maximum and therefore fails to describe fiber populations oriented at multiple directions within a voxel. When structures in complex tissues need to be understood, a high angular resolution diffusion imaging method should be used.

2.2.2 Diffusion Spectrum Imaging

Diffusion Spectrum Imaging (DSI) is a particular application of diffusion weighted MRI that aims to extract the complete ensemble average probability density function (PDF) of diffusing hydrogen atoms in a voxel of tissue. The PDF, which simply

21

maps the likelihood that a particle has diffused a particular distance and direction, reflects the tissue microstructure within the voxel. Directions of greatest diffusion are expected to correspond to the orientation of the long axis of fiber-like cells. These methods, described in brief in the next few paragraphs, have been previously used to image the myoarchitecture of the bovine tongue, and track neurons in brain tissue [85, 24].

The PDF is represented by a mathematical expression termed the average diffusion propagator $(\bar{P}_s)$, which is the sum of the probability density functions for each possible proton spin position and weighted by the proton density distribution. Stejskal and Tanner [70] [71], related $\bar{P}_s(\vec{R}|\Delta)$ to the amount of signal attenuation for an applied diffusion weighting gradient $\vec{g}$ and duration δ:

$$M(\vec{q}, \Delta) = M(\vec{0}, \Delta) \int \bar{P}_s(\vec{R}|\Delta) e^{(i\vec{q} \cdot \vec{R})} d\vec{R}, \qquad (2.2.2)$$

$$\vec{q} = \gamma \vec{g} \delta. \qquad (2.2.3)$$

Where $\vec{q}$ is called the q-value, γ is the proton gyromagnetic ratio, M is the signal intensity, Δ is the diffusion time, and $\vec{R}$ is the diffusion distance. The b-value defines the maximum diffusion weighting for a set of diffusion weighted image acquisitions:

$$b = \|\vec{q}_{max}\|^2 \Delta. \qquad (2.2.4)$$

Equation (2.2.2) shows that a Fourier relationship exists between the diffusion weighted signal in q-space and the three-dimensional probability distribution function. As shown in Figure 2.2.3, in DSI, diffusion weighted images are acquired for a sphere of q-values with indexed positions in a Cartesian grid in q-space and the PDF is reconstructed directly by the following:

$$PDF = F^{-1}(M(\vec{q})) \qquad (2.2.5)$$

where F^{-1} denotes the inverse Fourier transform. To reduce the data from a 3D image volume to a contour surface, the PDF is integrated radially and weighted by

the magnitude of $\vec{R}$:

$$ODF = \int \bar{P}_s(\rho\hat{u}|\Delta)\rho\hat{u}d\rho \qquad (2.2.6)$$

where ρ and $\hat{u}$ are the magnitude and unit vector describing $\vec{R}$. The result, normalized by the minimum and maximum diffusion for each voxel, theoretically describes the underlying fiber architecture and is termed the orientational distribution function (ODF).
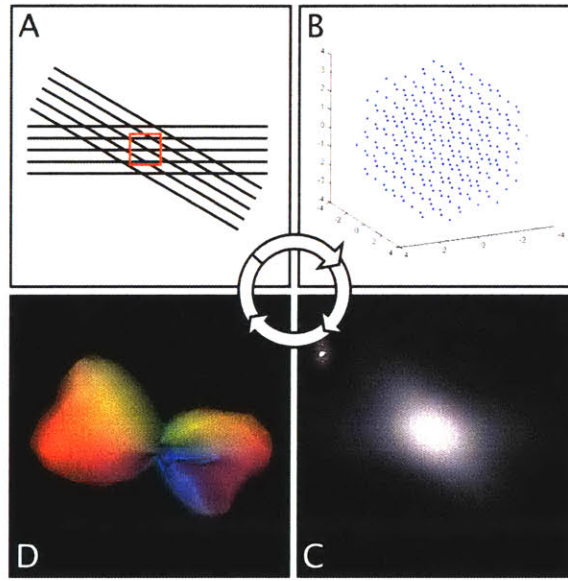
Figure 2.2.3: Derivation of fiber alignment from diffusion spectrum imaging. To extract multiple fiber directions within a voxel (A - red square), diffusion spectrum imaging first acquires a diffusion weighted signal for an indexed array of gradient directions and magnitudes in q-space (B). Then, through the fourier relationship, the probability density function is found (C). Lastly, radial integration provides an orientational distribution function which mimics the subvoxel fiber alignments (D).

2.3 Tractography

Streamline construction through tractography generates multi-voxel scale tracts along vectors corresponding to directions of maximal diffusion in each voxel. These data are derived solely from the principal eigenvector for each voxel, and thus ignore the degree of diffusional anisotropy.

Mathematically a streamline is defined to be tangent to a vector field at all points.

$$\frac{d\vec{S}(s)}{ds} = \vec{v}(\vec{S}(s))$$

(2.3.1)

where $\vec{S}(s)$ is the streamline, s is a path coordinate along $\vec{S}$, and $\vec{v}$ is the vector field. We create the streamline vector field from the set of eigenvectors corresponding to the largest eigenvalue of the diffusion tensor for each voxel. In the present experiments, tractography definition employed an approach called fiber assignment by continuous tracking (FACT) in which the vector field is assumed to be continuous rather than discrete [46]. The method operates by adding an angular threshold constraint for intervoxel connectivity. If the angular difference between the incoming streamline and the vector field of a particular voxel exceeds the threshold, the tract will stop. In the current work, we employed an angular threshold of $\pm 35°$ to define tract continuity. Streamlines were seeded at the center of every voxel and traced in both directions. Tractography visualization employed TrackVis, custom software developed using VTK, an open source 3D visualization tool (http://www.vtk.org/).

Chapter 3

Multi-scalar architecture

The power of diffusion weighted magnetic resonance imaging (DW-MRI) is to conveniently probe three-dimensional microstructure at an intermediate scale or *mesoscale*. In this chapter we explore this mesoscale by imaging a mouse tongue with both high field diffusion spectrum imaging (DSI) and with two-photon microscopy (TPM). DSI reveals whole tissue myoarchitecture from a top-down approach while TPM approaches from below by imaging individual cells with submicron pixel resolution.

The goal of this chapter is to elucidate more clearly the relationship between the observed diffusion function and characteristics of tissue microstructure. Cell membranes, the cytoskeleton, and sub-cellular components, restrict the motion of water molecules and thereby affect the directionality of diffusion. DSI theoretically allows the direct reconstruction of the probability density function (PDF) for a voxel of tissue. The PDF simply maps the likelihood of any particle to move a certain distance and direction. It has been generally confirmed that directions of enhanced diffusion in the PDF correlate to fiber direction [42], but the PDF may also contain much more information about the microstructure. Characteristics such as compartment size and surface permeability might even be more useful than the fiber direction. The ability to describe multiple compartment sizes could even be possible in biological tissue as has been done in synthetic porous media [45, 48]. The problem currently restraining us from inferring more than fiber direction from diffusion data is mainly a lack of understanding of the precise biophysical barriers involved and their relative

contributions to diffusional anisotropy. The roles of surface relaxation due to inelastic collisions, surface permeability, and cellular transport remain a mystery [79].

The tongue was selected for this study because it consists of a complex array of variably aligned fibers. In this tissue, the comparison of DSI with with TPM will allow:

- a more rigorous validation of DSI's capability to extract multiple fiber directions accurately within a voxel of tissue,

- a comparison of the DSI derived PDF to physical dimensions of the microstructure,

- a detailed visualization of the muscular anatomy of the mouse tongue.

A few technological advancements have allowed this comparison to be made. Whole tissue two-photon microscopy was made possible with the development of high throughput 3D tissue multiphoton imaging system (10 frames per second) with computer-controlled specimen stage and microtome. Additionally incremental hardware and software improvements have brought the resolution of high field DW-MRI to become commensurate with a TPM field of view (FOV).

The orientational distribution function (ODF) is hereby proposed as the mesoscale template for contractility that links the microscopic and macroscopic scales (Figure 3.0.1). DSI data is 7D; for each 3D voxel there is a 3D probability density function with a scalar value at each point. For easier visualization, the dimensions are reduced by radially integrating from the center of each PDF, resulting in a set of ODFs. Similarly, the principal patterns in the microscopy data were revealed by radially integrating from the center of the autocorrelation data. The local maxima of the ODFs for each method were identified and compiled into a vector field. In this manner, mesoscale tractography was performed from both the exact fiber orientation obtained by microscopy and that obtained by DSI of the whole tissue, thus providing a spatial linkage at the mesoscale.

The generation of tractography representation of myoarchitecture from the two completely separate methods allows visual co-registration. Once co-registered, the
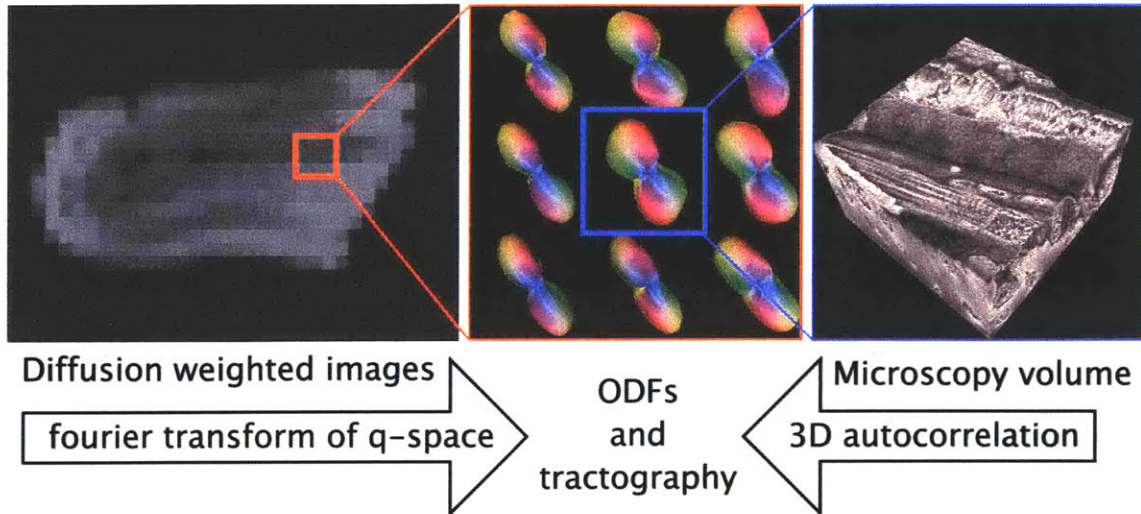
Figure 3.0.1: Mesoscale tractography: Template for contractility at the interface of microscopic and macroscopic scales. To quantitatively relate myofiber architecture at the resolution of the cell and the tissue, voxel specific ODFs and intervoxel tracts were generated. A set of diffusion weighted images leads to the extraction of subvoxel information about fiber alignment in the form of an ODF field, whereas an ODF field can also be generated directly via the 3D autocorrelation function of the microscopic image.

predicted structure based on diffusion can be directly compared to the underlying microstructure. Combining knowledge of the physical dimensions with simulations of restricted diffusion experiments, it may be possible to draw conclusions about the precise origin of diffusional anistropy; thus providing a means to extract additional useful information from diffusion spectrum imaging in biological tissue, such as compartment size and membrane permeability.

3.1 Methods

3.1.1 High field diffusion spectrum image of mouse tongue

Whole anterior tongues from female 357BL or FYDR-Rec mice (n=3) were scanned with a Magnex Scientific $9.4\ T$ $2\ cm$ diameter horizontal bore magnet with Magnex gradient coil set capable of $20\ G/cm$. The imaging protocol employed a diffusion gradient sampling scheme, which consisted of a key-hole Cartesian acquisition to

include q-space values lying on a Cartesian grid within a sphere for a total of 515 sampling points. With a max b-value of $7000s/mm$, voxel size was $150 \times 150 \times 150 \mu m^3$, and TR 1200 ms, the entire acquisitions required 22 hours to complete.

3.1.2 Whole tissue two-photon microscopy and autocorrelation analysis

Two-photon image acquisition

Whole anterior tongues from female 357BL (n=2) and FYDR-Rec mice (n=1) were imaged using a multi-focal multi-photon high speed imaging system with a robotic sample stage and an automated microtome. Prior to scanning, excised tissue samples were fixed in buffered neutral 10% formalin within 1 hour of harvest, and embedded in paraffin within 1 day by the Brigham and Women's Hospital Department of Pathology.

Two photon microscopy was achieved using a custom-built microscope and acquisition software [37, 40]. The light source for two-photon excitation was a commercial Ti:Sapphire laser, Mira (Coherent, Santa Clara, California, United States), pumped by a 10-W solid-state laser delivering $150fs$ pulses at a rate of $80MHz$ with the power delivered to the objective ranging from $100-250\,mW$ depending on imaging depth. The excitation wavelength was set to $890\,nm$, with the excitation signal passing through an Achroplan $40 \times /0.8$ NA water-immersion objective (Zeiss, Oberkochen, Germany) and collected after a barrier filter by a photomultiplier tube. Figure 3.1.1 shows an example of TPM raw data

Autocorrelation image analysis

Analysis of microscopic FOV was accomplished using an autocorrelation algorithm to extract main fiber directions for each 3D field of view. The 3D autocorrelation was found by taking the Fourier transform of image volume, performing component by component multiplication by its own complex conjugate and inverse transforming back into real space.
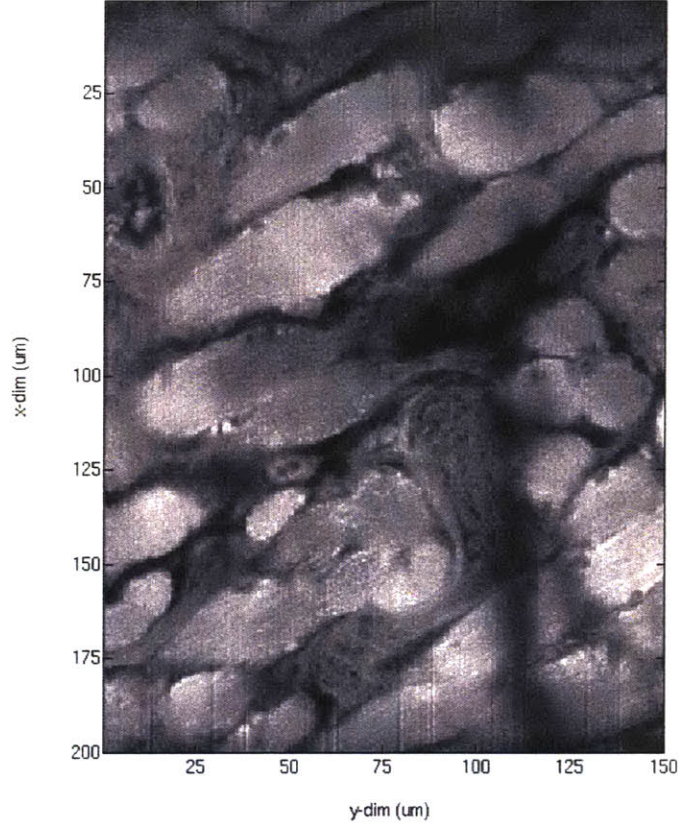
Figure 3.1.1: Single slice example of the two-photon data set. Above images were acquired for an entire mouse tongue. Each field of view (FOV) dimensions were $150\ \mu m \times 200\ \mu m \times 80\ \mu m$. Adjacent FOV had $30\ \mu m$, $40\ \mu m$, and $20\ \mu m$ of overlap in each dimension repectively. Resolution in the xy dimension was $0.5\ \mu m$, and z-dimension was $2\ \mu m$

$$Acorr = F^{-1}(G \cdot \bar{G}) \tag{3.1.1}$$

Where F^{-1} denotes the inverse fourier transform, G is the 3D fourier transform of the image volume, and $\bar{G}$ is the complex conjugate of G. Each FOV was divided into 4 unique image volumes with dimensions $80 \times 60 \times 60\ \mu m^3$. The image volumes were first linearly interpolated in the z direction to give isotropic voxel resolution and windowed with a Kaiser window to reduce edge effects. A frequency filter was applied to remove those features with a wavelength greater than or equal to $120 \mu m$. The main patterns in the microscopy data are revealed by radially integrating from the center

of the autocorrelation data, thereby creating an ODF similar to that created for each voxel using diffusion spectrum MRI. A single value was recorded for the bidirectional radial integration for the set of 181 vectors equally spaced on the surface of a half-sphere over a distance of 12.5 μm with a stepsize of 0.05 μm; thus compressing each 9.2 megabyte image volume file into a single vector with 181 components.
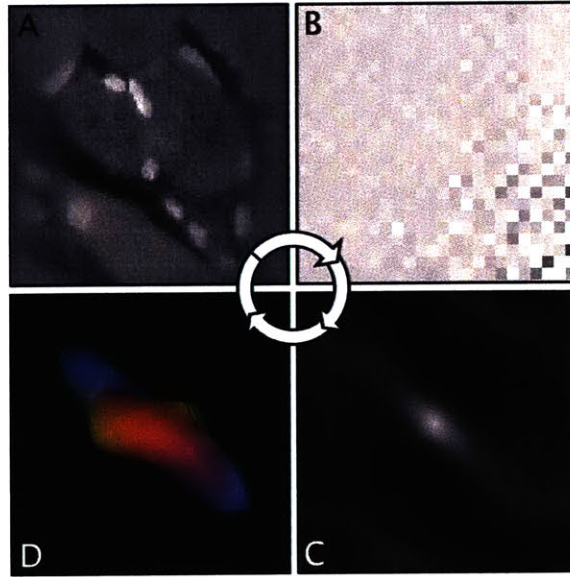
Figure 3.1.2: Derivation of fiber alignment from two-photon microscopy. To summarize fiber directions within a TPM field of view, an autocorrelation is performed: First the data by windowed with a Kaiser window (A) to reduce edge effects, then by the 3D Fourier transform, the data is expressed in frequency space (B) and a frequency filter applied to remove patterns with a wavelength greater than or equal to twice the FOV. The 3D Fourier tansform is then multiplied by its own complex conjugate to obtain the autocorrelation (C). Lastly, radial integration provides an orientational distribution function which describes fiber alignments.

3.1.3 Orientational distribution function and tractography

Both DSI and two-photon microscopy autocorrelation result in an ODF summarizing the fiber orientation within block of tissue. Although they are informative, overall fiber architecture is often difficult to infer from looking at ODFs alone. A vector field was created from the local maxima of each ODF and streamline tractography performed. Tractography is an intuitive visualization method that creates connections based on angular similarity of adjacent voxels (Section 2.3). The current images

employed a 35° angular threshold to generate intervoxel tracts. It should be empha-
sized that the tracts so constructed do not represent actual anatomical entities, such
as fiber bundles or fascicles, but indicate a set of macroscopically related diffusion
maxima corresponding to a set of similarly aligned muscle fiber populations.

3.2 Results

3.2.1 Myoarchitecture of the murine tongue

The mouse tongue is surprisingly complex. Depicted in Figure 3.2.1 is the normal
myoarchitecture of the excised anterior murine tongue obtained by DSI, demonstrat-
ing in particular the predicted relationship among the intrinsic fiber populations and
novel observations regarding the configuration of the transversus fibers and the inser-
tion points for the extrinsic fiber groups. Of the extrinsic muscles, the genioglossus
(gg) is the most clear, entering from below and extending along the sagittal plane into
the lingual core. The laterally located green fibers wrapping superiorly as they ap-
proach the anterior tip could either be the ends of an inferiorly positioned styloglossus
or perhaps the mouse equivalent of the chondroglossus.

3.2.2 Visual co-registration of diffusion and microscopy trac-
tographies

We show in Figure 3.2.2 a direct comparison of tractography renderings (sagittal ori-
entation) from DSI and from two photon microscopy for the mouse anterior tongue.
Observe the high degree of concordance in terms of the distribution of myofiber tracts.
The ability to identify the cells comprising a region of mesoscale architecture is signifi-
cant since it provides a direct anatomical validation for DSI tractography and provides
a method for relating structural data at the cellular level with morphogenesis at the
scale of the tissue.

31
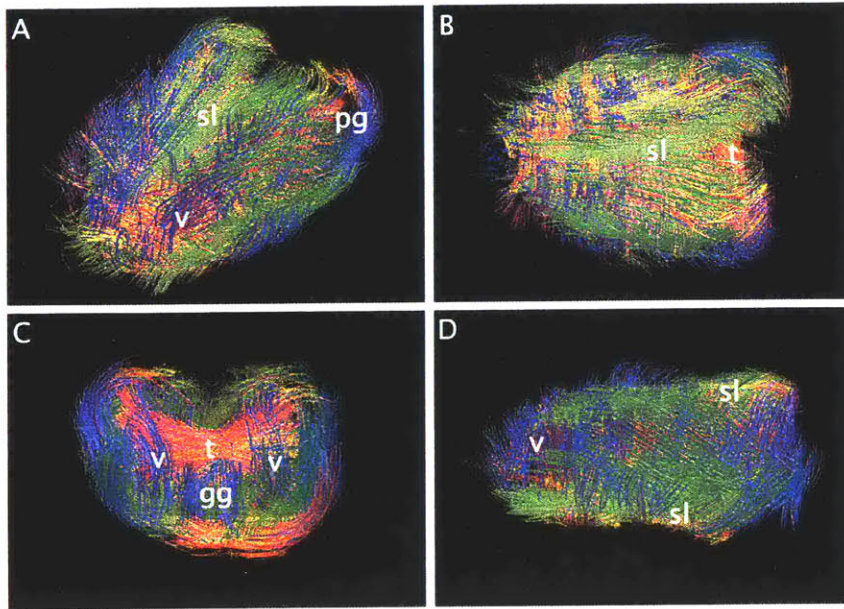
Figure 3.2.1: DSI of murine tongue. Demonstrated is a full diffusion spectrum imaging with tractography data set obtained at 9.4 T (voxel size 150 μm) of the anterior 357BL mouse tongue from the (A) oblique, (B) coronal (superior), (C) axial (posterior),and (D) sagittal perspectives. The green superior longitudinalis (sl) and inferior longitudinalis (il) run along the dorsal and ventral exterior surfaces. The transversus (t) and verticalis (v) are not perfectly horizontal and vertical but rather form an interesting concave box like structure, becoming parallel with each other at the corners. Extrinsic fibers identified include the genioglossus (gg) and palatoglossus (pg)

3.3   Discussion

The compilation of TPM data into a visualization of overall tissue architecture is in itself a useful accomplishment. Currently efforts are focus on computational alignment of adjacent FOV to correct for the around $\pm 5\,\mu m$ accuracy of the mechanical stage. The method described in this paper provides a less computation intensive alternative which identifies interconnectivity, yet ignores possible FOV missalignment. Whole tissue architecture derived by TPM via autocorrelation analysis and visualized using TrackVis (software developed for viewing diffusion weighted MRI tractograpy data - http://trackvis.org) may even be more convenient and adept for certain applications than a precisely aligned montage.

The architectures found using DSI and TPM exhibit very similar features (i.e longitudinalis sheath, crossing intrinsic muscles in lingual core, location and inser-
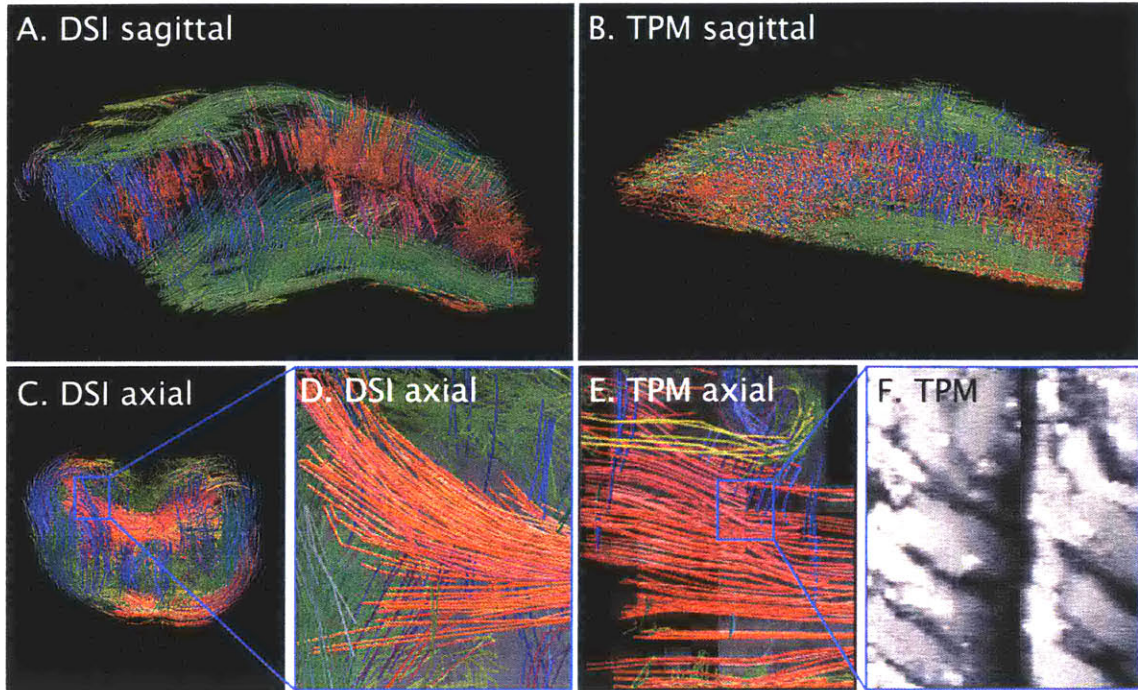
Figure 3.2.2: Comparison of mesoscale tractography rendering derived from diffusion spectrum imaging (DSI) and two-photon microscopy (TPM). Upper row: Tractography of mouse tongue myoarchitecture (sagittal orientation) obtained by DSI (A) and TPM (B). The most lateral slices of the DSI tractography have been removed to match the TPM. DSI tractography image (C) of an axial slice, and a close-up (D), emphasizing the transverse oriented fibers. Similar resolution TPM tractography image is displayed (E) accompanied by a TPM image in (F) of a region of myocytes corresponding to the indicated myofiber tracts shown in (E, blue square). These results confirm the capacity of these imaging methods to derive intermediate scale myofiber tracts both from the local diffusion maxima displayed by DSI and directly from 3D microscopy data.

tion angle of genioglossus), although no quantitative co-registration has yet been performed.

The comparison of the diffusion function with the autocorrelation function is interesting because, theoretically, for the long diffusion time limit in cells with perfect boundaries, the diffusion-derived PDF would be identical in form to the autocorrelation intensity distribution [79]. The fact that the width of the PDF at its narrowest dimension should be equivalent to twice the fiber diameter was confirmed by theoretical analysis and computer simulations of unrestricted and restricted diffusion experiments were performed. though these simulations should be built upon to ac-

count for semipermeable membranes and cell walls, as well as intricacies of DW-MRI.

The probabillity distributions from the raw DW-MRI data were reconstructed for several voxels in the lingual core in a continuous method as to preserve physical dimensions. Figure 3.3.1 shows an intensity image of the PDF calculated discretely according to the inverse fourier transform relationship described in Section 2.2.2. The other three plots show three linear continuous probability distributions along the three eigenvectors of the hessian matrix describing the 3D PDF at the origin. The hessian matrix is defined as:

$$\mathbf{H} = \begin{vmatrix} I_{xx} & I_{xy} & I_{xz} \\ I_{yx} & I_{yy} & I_{yz} \\ I_{zx} & I_{yz} & I_{zz} \end{vmatrix}, \tag{3.3.1}$$

where I is the intensity of the PDF at a point in diffusion space and is equal to the following for the sum over all 515 points acquired in q space. Only the symmetric and real components are considered.

$$I = \frac{1}{\sqrt{\pi}} \sum_{i=1}^{515} E(\vec{q}(i)) \cos(\vec{q}(i) \cdot \vec{r}), \tag{3.3.2}$$

where E is the signal intensity of the voxel at the specified gradient vector, $\vec{q}$, and $\vec{r}$ is the vector describing a location in diffusion space. I_{jk} is the second partial derivative of I with respect to the identified axes j and k. At the origin, this can be written as:

$$I_{jk} = \frac{\partial^2 I}{\partial j \partial k} = -\frac{1}{\sqrt{\pi}} \sum_{i=1}^{515} E(\vec{q}(i)) q_j(i) q_k(i), \tag{3.3.3}$$

where q_j and q_k are the j and k components of $\vec{q}$. The linear probability distributions along the eigenvectors were calculated using Equation 3.3.2.

The eigenvector corresponding the smallest eigenvalue of the Hessian matrix should correspond to the narrowest width of the PDF. From the plots in Figure 3.3.1, one can see that the dimensions of the PDF along the tertiary eigenvector are approximately $10\mu m$, though the lack of sampling at high spatial frequency makes the reconstruction

34

very wavy. Additionally, the value obtained for estimated diameter is not very close to the actual cell diameters observed in Figure 3.1.1, which are closer to 20 to 25 μm. There are many possible explanations for the discrepancy; such as subcellular components hinder diffusion, or the short diffusion times used in the pulse sequence do not allow definition of such large distances. Much more effort should be concentrated on these analyses.
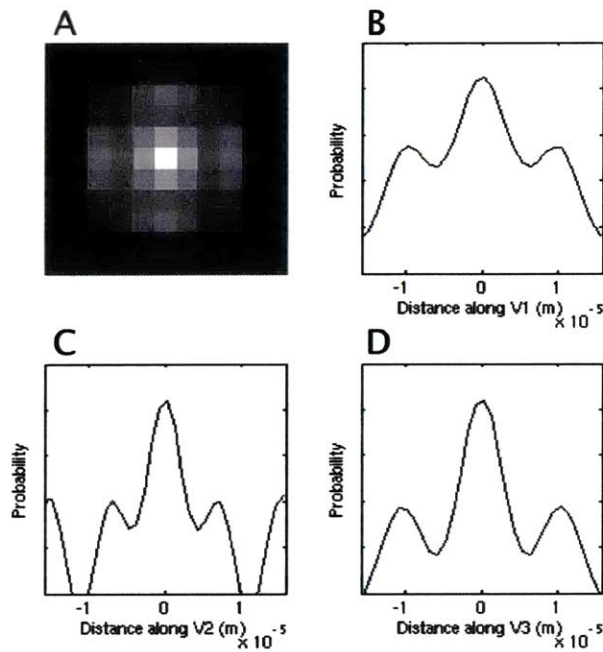
Figure 3.3.1: Dimensions of the DSI probability distribution function for typical voxel in lingual core. (A) Middle slice of discretely calculated 3D probability distribution function. (B) Continuous probability distribution along V1, primary eigenvector of the hessian matrix describing center voxel, (C) Continuous PDF along V2 and (D) Continuous PDF along V3 (the secondary and tertiary eigenvectors respectively). The width of the narrowest (V3) distribution should correspond to twice the cell diameter in uniformly oriented tissue.

One issue discovered during this experiment was that the tissue being studied must not contain fluorescent cells. The specimens obtained were from mice being used in an unrelated experiments. Most were wild type, but some were FYDR-Rec (Fluorescence Yellow Direct Repeat - Recombined), which is a trangenic mouse that expresses EYFP proteins. These mice were injected with Hoechst, a nucleus-staining dye, just prior to sacrifice. It was discovered that the lingual myocyte nuclei exhibited

fluorescence as well. The high signal from nuclei resulted in poorer definition of cell boundaries and disrupted the extraction of fiber direction by the autocorrelation algorithm. This appeared to cause an increase in the bias towards selecting maxima in the x, y, and z orthogonal directions.

In conclusion, derivation of 3D fiber orientation through two complimentary imaging methods was performed on whole mouse tongues, a tissue consisting of complex arrays of variably aligned fibers. We compared mesoscale myofiber tracts derived from magnetic resonance DSI, which probes microstructure at a multi-cellular scale based on the preferential diffusion of water in the presence of microscopic barriers, and TPM, which images individual cells with submicron resolution. DSI was performed at $9.4\,T$ (b-value 7000 s/mm and 150 μm isotropic voxels) and multivoxel tracts generated on the basis of angular similarity. TPM was performed with a high throughput 3D tissue multiphoton imaging system (10 frames per second) with computer-controlled specimen stage and microtome, and myofiber tracts generated from autocorrelation analyses of individual fields of view. Computational simulations were performed to model restricted diffusion to infer compartment size, i.e. fiber diameter. These data revealed a consistent relationship between the dimensions of the diffusion probability density function and characteristics of tissue microstructure, and the virtual super-imposition of the distributed mesoscale myofiber tracts. The identification of the cells comprising mesoscale myoarchitecture provides a direct anatomical validation for DSI tractography and a method for relating information at the cellular level with morphogenesis of tissues.

Chapter 4

In vivo: lingual myoarchitecture and local mechanics

In this chapter we demonstrate how MRI methods can be applied in vivo to study complex muscle architecture and its relation to mechanics. The tongue was selected for study because of its accessibility by surface coils, relative freedom from motion due to respiration and heart beats, and for its well known structural intricacy. We first explain the concept of crossing fibers and hydrostat function, then explain how diffusion derived myoarchitecture and strain rate imaging were used to study the propulsive phase of the swallow. This application of technologies is new and has brought diffusion imaging of myoarchitecture closer to clinical application.

4.1   Muscular hydrostats

A muscular hydrostat is a body or appendage, consisting almost entirely of muscle, that both creates motion and provides structural support for that motion. The entire body of an organism may be a muscular hydrostat, as are the bodies of some worms, or the muscular hydrostat may be an appendage originating from a bony prominence, such as the tongue and elephant trunk.

To illustrate what is meant by the term muscular hydrostat, let us consider a highly simplified model of a non-muscular hydrostat, the well-known water balloon.

We know intuitively this objects key mechanical properties, that is, highly elastic rubber-constituted walls and aqueous contents. which by its isotropic nature allows the balloon to deform equally in all directions in response to the application of pressure. As shown in the first row of Figure 4.1.1, pressure applied from any single direction will result in passive compressive deformation of the balloon in that direction and commensurate expansion in the two orthogonal directions. Extending this concept, passive compression of the balloon from two directions simultaneously will result in commensurate expansion in the remaining direction. A muscular hydrostatic tissue differs from this simplified balloon model in two fundamental ways: 1) The internal structure of the tissue is not homogeneous, but rather is comprised of narrow and elongated anatomical units, i.e. muscle fibers, surrounded by a relatively inflexible interstitium. The tissue will thus deform preferentially along the long axis of the muscle fibers, rather than transverse to the long axis of the fibers. 2) Deformation of a muscular hydrostat results from shortening, i.e. contraction, along the long axis of internally located muscle fibers, or stretching, i.e. elongation, of the tissue resulting from the contraction of externally located muscle fibers. As a result, a muscular hydrostat is constrained in the manner in which it may deform by the orientation and contractile properties of its constituting fibers, a property termed anisotropic deformation. If we now consider a muscular tissue whose fibers are all aligned in the same direction (second row of Figure 4.1.1), such as the skeletal muscle of the extremities, such as tissue has the capacity to compress with fiber shortening only along the long axis of its fibers and to expand only in directions orthogonal to the long axis of its fibers. On the other hand, if we consider a tissue whose fibers are crossed orthogonally to each other, such as the core region of the mammalian tongue (third row of Figure 4.1.1), it is capable of compressing or expanding in one or multiple directions, depending upon the extent to which particular fiber populations are involved, to generate localized stiffening and/or displacements associated with speech and swallowing.

Hydrostatic deformation is associated with the juxtaposition of muscle fiber arrays obliquely oriented to each other, at both the microscopic and macroscopic scales. The
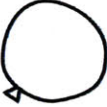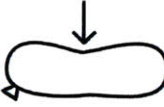
Type	Example	Possible configurations		Total
		Rest	Deformations	
isotropic	water balloon		↓	NA
aligned one way	bicep		x1	2
aligned two way	lingual core		x2 / x1	4
aligned three way	anterior tongue		x3 / x3 / x1	8

Figure 4.1.1: The concept of a muscular hydrostat is defined in this figure. Given the presence of local anisotropy in a muscular tissue, the complexity of fiber alignment determines the number of possible deformations attainable.

existence of crossing fibers allow for the possibility of synchronized multi-directional contraction and isovolemic deformation. The results of this model demonstrate that synergistic contractions of fibers at orthogonal or near orthogonal directions to each other is a necessary condition for volume conserving deformation. In conclusion evidence is provided in support of the supposition that hydrostatic deformation is based on the contraction of orthogonally aligned intramural fibers functioning as a mechanical continuum.

We present in Figure 4.1.2 a series of conceptual drawings indicating which muscles might contribute to the formation of several prototypical shapes, namely, anterior directed protrusion, bolus accommodation during swallowing, and retrograde bolus

propulsion during swallowing. In each case, the deformations are depicted from the sagittal, anterior coronal, and posterior coronal perspectives. In each instance, the specific deformation is described from the perspective of contributions of intrinsic and extrinsic fiber populations, and is viewed in the context of its hydrostatic properties. The fact that the tissue embodies fibers with extensive and complex crossing patterns emphasizes that the tissue is capable of compression or expansion in one or many directions based on the specific fiber populations which are active.
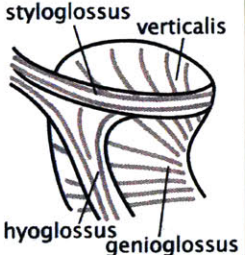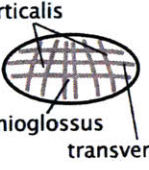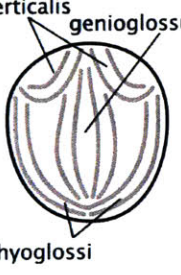
Tongue section	Rest configuration	Prototypical Deformations
sagital	styloglossus verticalis hyoglossus genioglossus	anterior protrusion bolus acommodation retrograde propulsion
anterior–coronal	verticalis genioglossus transversus	anterior protrusion bolus acommodation retrograde propulsion
posterior–coronal	verticalis genioglossus hyoglossi	anterior protrusion bolus formation retrograde propulsion

Figure 4.1.2: Conceptual drawings depicting the way in which synergistic contractions involving the intrinsic and extrinsic muscles may contribute to prototypical deformations, namely anterior protrusion, bolus accommodation during swallowing, and retrograde propulsion during swallowing.

Anterior protrusion appears to result principally from the synchronous contraction of the tranversus and verticalis fibers. The role of the genioglossus in this rather

simple deformation is controversial, but in general it appears to be less important in humans as compared to other mammalian species for which forceful extension and manipulation of the tongue is critical for obtaining food. The process of bolus accommodation is important for all mammalian species for forming the ingested morsel of food into a bolus, which then may be propelled retrograde in the course of swallowing. The exact method by which bolus accommodation is accomplished thus defines the physical limits of oral ingestion and embodies important species specific functionality. In this regard, note the prominent role believed to be exerted by graded contraction of the midline genioglossus fibers in humans, while also acknowledging the contribution of intrinsic fibers towards the stiffening and broadening the bolus accommodating concavity. Lastly, let us consider the complex set of events contributing to the rapid and forceful reconfiguration of the tongue as it facilitates bolus movement from the oral cavity to the pharynx. Given the diverse forms and sizes taken by the bolus, it is reasonable to postulate the involvement of multiple synergisms involving at varying orientations to each other. It might reasonably be predicted that retrograde lingual propulsion involves the coordinated actions of the genioglossus, hyoglossus, styloglossus merging with the inferior longitudinalis, as well as the stiffening effect of bidirectional contraction of the core lingual fibers. The precise delineation of which muscles contribute to specific functional deformations of the tongue and to what degree they are active in modulating adaptive lingual mechanics will require considerable further research.

4.2 Myoarchitecture of the human tongue

The tongue is an intricately configured muscular organ, which is responsible for the manipulation and transport of food in the oral cavity during swallowing, as well as the subtle variations in shape and stiffness needed for human speech. The tongues myoarchitecture consists of a large array of variably aligned and extensively interwoven intrinsic (without attachment to bony surfaces) and extrinsic (with attachment to bony surfaces) muscles. The intrinsic musculature consists of a core region of

41

orthogonally-aligned fibers, contained within a sheath-like bundle of longitudinally oriented fibers. The intrinsic fibers are delicately merged with extrinsic muscles that modify shape and position from a superior direction (palatoglossus), posterior direction (styloglossus), and inferior direction (genioglossus and hyoglossus). It is generally believed that these fibers function synergistically to constitute a near limitless number of physiological deformations.

To visualize the complex myoarchitecture of the tongue this experiment employed MRI sensitized to the directionality of water diffusion [70, 39]. Diffusion weighted imaging has the capacity to resolve anisotropic particle movement, and thus infer fiber organization at a voxel scale in biological tissue [4, 27, 30, 47, 87]. The anisotropy of water diffusion in skeletal muscle in particular has been demonstrated and anatomically validated [8, 31, 32, 82, 10]. In the ex vivo bovine tongue, diffusion tensor fields were exploited to produce a virtual anatomical displays [25, 83]. Acknowledging the limitations of a diffusion tensor to describe fiber alignment in the context of intravoxel fiber crossing or divergence, lingual myoarchitecture in excised tissue was imaged with diffusion spectrum imaging (DSI), a method which depicts complex fiber relationships in terms of the multimodal behavior of a probability distribution function (PDF) and the multivoxel associations of the local diffusion environments were represented with tractography [26, 22]. In the aggregate, these studies allowed for the reconsideration of lingual myoarchitecture in terms of macroscopic tract-like structures that constitute an anatomical template for local tissue deformation. The logical extension of this approach to the in vivo realm should allow correlation of macroscopically resolved myofiber tracts with local deformation in humans. The use of DSI in vivo, however, is compromised by poor signal-to-noise related to short allowable imaging times. As an alternative approach, we employed multiple gradient direction diffusion tensor imaging (DTI) with tractography. While lacking the ability to resolve intravoxel crossing fibers, DTI tractography may well have the capacity to resolve intervoxel crossing and non-crossing fibers at scales which are relevant since they coincide with the practical dimensions of mechanical deformation.

Several investigators have previously used DTI techniques to image cardiac [62,

42

61. 78. 12. 20] and skeletal muscular tissue in vivo [67. 19. 69. 23]. In the current study, we have modified our approach in several specific ways: First, we employed an increased number of different diffusion sensitizing gradients to improve angular precision [56, 34]. Second, to reduce potential bias in the more heterogeneously oriented tissue of the tongue, we used isotropic voxels. Third, for improved SNR in the region of interest, two surface coils were used with overlapping sensitive volumes. Lastly, we incorporated the method of tractography to provide data of intervoxel geometric association, and thus allow important structure-function inferences. Our results demonstrate the feasibility of resolving the highly complex anatomical relationships characteristic of the human tongue using DTI tractography.

4.2.1 Methods for in vivo DTI tractography

The lingual myoarchitecture of 5 normal human subjects was investigated using DTI tractography. Subjects were instructed to attempt to refrain from motion during each scan and to position the tongue in the oral cavity in a naturally occurring configuration. thus minimizing the air space around the tongue. Data was acquired using a $1.5\,T$ system (Avanto, Siemens Medical Systems, Erlangen, Germany) equipped with two custom-built surface coils, each approximately $60\,mm \times 60\,mm$. The surface coils were mounted on thin plastic sheets, placed flush against each cheek and gently secured. In this study. we employed a twice-refocused spin echo DTI pulse sequence to reduce eddy current distortions [60]. The pulse sequence incorporated standard single shot echo-planar (EPI) spatial encoding. Imaging parameters were as follows: TR = $3\,s$, TE = $80\,ms$. field of view $192\,mm \times 192\,mm$, 24 slices. $3\,mm$ slice thickness. A b-value of $500\,s/mm^2$ was chosen to give adequate diffusion weighting while retaining a sufficiently high signal-to-noise ratio. Diffusion-weighting gradients were applied in 90 unique directions in addition to 15 non-diffusion weighted volumes. Complete tongue acquisitions were accomplished in $5\,min$, $15\,s$.

Streamline construction through tractography was employed to generate multi-voxel scale tracts along vectors corresponding to directions of maximal diffusion in each voxel. In the current work. we employed an angular threshold of $\pm 35^\circ$ to define

43

tract continuity.
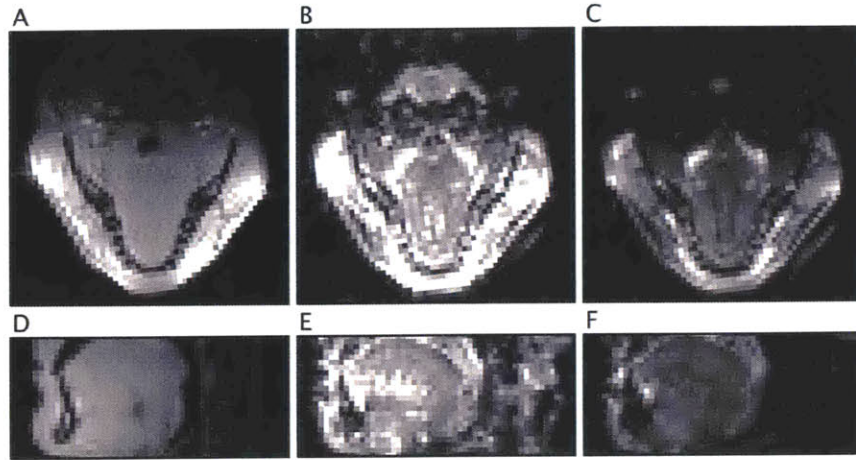
Figure 4.2.1: Examples of raw diffusion weighted image data. Images show an axial and a sagittal slice acquired with a typical anatomical pulse sequence (A and D), an approximately zero b value EPI (B and E), and a diffusion weighted EPI (C and F). The darker regions within the tongue body in the diffusion weighted images signify greater diffusion in the direction of the applied gradient. Diffusion weighted images used a twice-refocused spin echo DTI pulse sequence with $\text{TR} = 3\,s$, $\text{TE} = 80\,ms$, field of view $192\ mm \times 192\ mm$, 24 slices, $3\ mm$ slice thickness, in 90 gradient directions with b-value $500\ s/mm^2$.

4.2.2   Results

Tractography images were created from the DTI dataset obtained for each subject. The images in this paper are derived from a single subject, and are representative of the data acquired for all 5 subjects. Partially transparent, low b-value, magnitude images are displayed for anatomical reference and to distinguish between tracks closer and further away from the point of view. The color-coding for the tracts is the same in all images, regardless of the slice orientation, and is as follows: green indicates tracts in the anterior-posterior direction, red indicates tracts in the transverse direction, and blue indicates tracts in the superior-inferior direction.

The complete lingual muscle DTI tractography overlaid with three orthogonal low b-value magnitude images is shown in Figure 4.2.2 from an oblique perspective (A) and from the superior (B) and left lateral (C) directions. Extraneous tracks separate from the tongue musculature were removed using slice filters. Since the extrinsic and

intrinsic muscles merge so thoroughly in the body of the tongue. identification of individual muscles is accomplished mainly by their points of attachment. The thick green track bundles on the lateral edges of the tongue that appear to project towards the styloid process correspond to the styloglossus (sg). The hyoid bone, unique in the human body because it does not articulate with any other bone, functions as the inferior connection for several extrinsic lingual muscles, including the hyoglossus (hg), and a posterior and inferior section of the genioglossus. Although it is the largest extrinsic muscle, the genioglossus (gg) is mostly obscured in these images due to its midline location. The palatoglossus (pg) originates superior to the tongue in the soft palate and curves laterally and anteriorly where it blends with the superior longitudinalis. The intrinsic muscles are less evident as discrete muscles in this image as they appear to merge with inserted extrinsic muscles. For ease of visualization, the following figures display only those tracts in contact with a designated reference planes or spherical regions of interest (ROIs), and thus only a subset of the complete dataset of tracts, are shown in each image.

We compare in Figure 4.2.3 a midline sagittal view of lingual musculature based on DTI tractography with an anatomical drawing of these same muscles obtained from Grays Anatomy (31). In general, lingual myoarchitecture derived from DTI tractography depicts both intrinsic and extrinsic myofibers and correlates closely with the underlying anatomy. The prominent blue and green fan-shaped structure (gg) corresponds to the genioglossus. The tracts originate from a mandibular attachment and spread in the posterior and superior directions, spanning nearly the entire profile of the tongue. Originating at the same bony attachment is a group of green horizontal tracts corresponding to the geniohyoid (gh) which continue only a short distance in the posterior direction and possess a significant downward curvature on both ends. The horizontal green tracts (sg) are consistent with the styloglossus approaching from the rear and merging with the inferior longitudinalis as it passes the hyoglossus (hg). Since DTI tractography allows only a single vector of maximum diffusion per voxel, the demonstration of intravoxel fiber crossing is not feasible. This condition may partially explain the relative scarcity of tracts in the anterior tongue. which contains a high
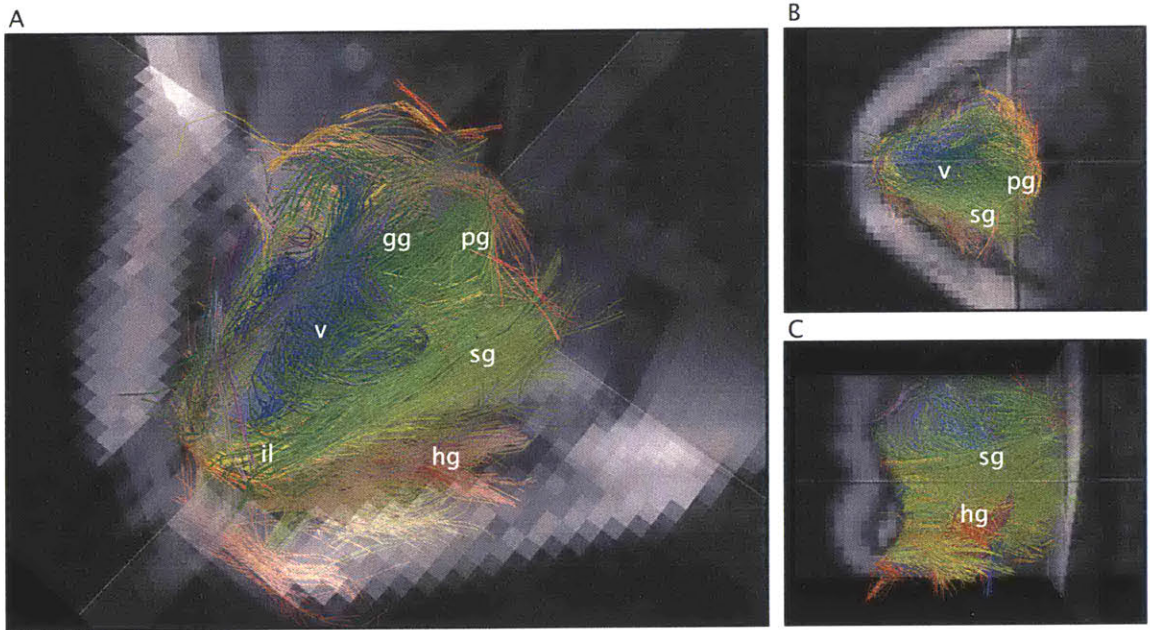
Figure 4.2.2: DTI tractography of human tongue (complete data set). Complete lingual muscle DTI tractography data set from an oblique perspective (A), and from the superior (B), and left lateral directions (C). Multivoxel tracts corresponding to the direction of maximal diffusion/voxel were constructed by the streamline method. Color-coding for the tracts is the same for all figures: anterior-posterior direction is green, transverse direction is red, and superior-inferior direction is blue. The styloglossus (sg), hyoglossus (hg), genioglossus (gg), and palatoglossus (pg) are identified as well as the merging of these muscles in the lingual core with the verticalis (v) and inferior longitudinalis (il). Three orthogonal low b-value magnitude images serve as anatomical reference. Dimensions [64,64,24], selected slices [x = 30-40, y = 1-34, z = 0-24], track length thresholds [$12\,mm - 140\,mm$].

proportion of orthogonally crossing fibers. Large fluctuations in the vector of maximal diffusion occurring in regions of intravoxel fiber crossing exceed the angular threshold for tract connectivity, and thus limit tract definition. To further assess the extent of intravoxel crossing in the anterior tongue, we measured average fractional anisotropy in the anterior versus the posterior mid-sagittal tongue. Fractional anisotropy (FA) may be represented as $FA = std(\lambda)/rms(\lambda)$, where λ is the set of eigenvectors of the diffusion tensor, std is their standard deviation and rms is their root mean square, and varies from 0 (perfectly isotropic diffusion condition) to 1 (diffusion along an infinite cylinder). By this analysis, the FA of the anterior tongue, similar to previous reports (32), was 0.174 whereas the FA of the posterior tongue was 0.289, or approximately

40 percent greater.
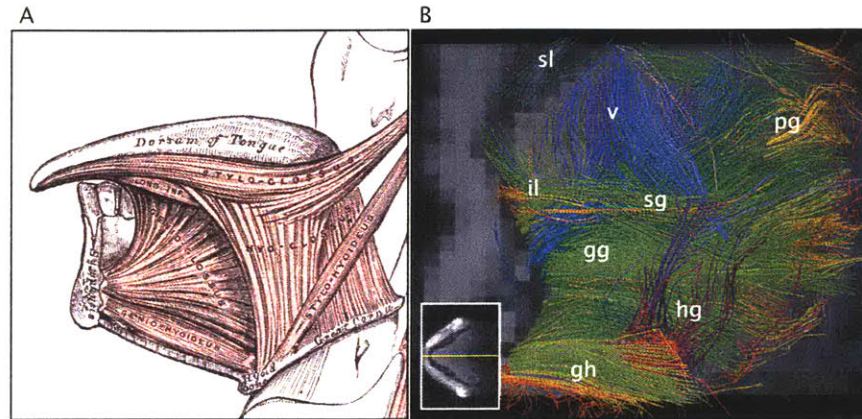
Figure 4.2.3: DTI tractography of human tongue compared with anatomical drawing (sagittal). Anatomical drawing obtained from Grays Anatomy [29] (A) is presented in comparison to a sagittal view of lingual myoarchitecture based on in vivo DTI tractography (B). Note the close structural correlation between genioglossus (gg), geniohyoid (gh), hyoglossus (hg), and styloglossus (sg) merged with the inferior longitudinalis (il). Not shown in the anatomical drawing, but visible in the tractography are the superior longitudinalis (sl) and verticalis (v) fibers in the anterior tongue, and the palatoglossus (pg) in the posterior tongue. Inset in left lower corner of (b) demonstrates slice location. Slice position shown in accompanying inset image. Dimensions [64,64,24], selected slice [x = 32], track length thresholds [$12\ mm - 140\ mm$].

The groups of tracts corresponding with three major extrinsic muscles (genioglossus, hyoglossus, styloglossus) were isolated and the average FA and average diffusion coefficient (ADC = trace(D)/3) calculated for all associated voxels. Intrinsic muscles could not be isolated because of the high degree of merging within the core of the tongue. Mean vector direction was calculated by summing the principle eigenvectors of every voxel touching a particular muscle tract group. Using the mean vector direction of the genioglossus as a reference for zero degrees yaw and accepting the anterior-posterior axis of the acquisition volume placement for zero degrees pitch, the mean values and standard deviations of ϕ and θ, as defined in Figure 4.2.4, were found for each major muscle tract group and displayed in 4.2.1. The mean vector directions relate to each muscle as a whole, and therefore may insufficiently describe local muscle architecture: either because orientation changes along its length, as in the styloglossus, or spans an angular range greater than 90 degrees, as in the genioglossus.

47
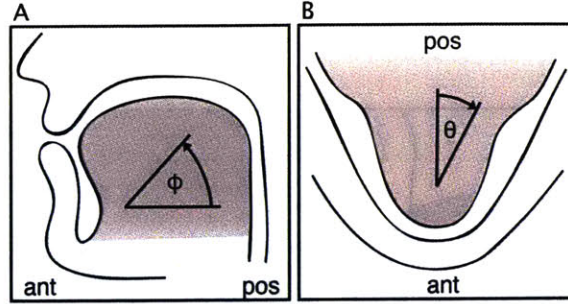
Figure 4.2.4: Definition of mean vector direction. Diagram demonstrating the polar coordinate system used to define mean vector direction for the three major extrinsic muscles in each of the five subjects. The sagittal view (A) shows ϕ, the angle at which the muscle intersects the horizontal plane. The axial view (B) shows θ, the angle at which the muscle diverges from the midline. For each subject, mean vector direction of the genioglossus was used as a registration reference for zero degrees yaw and the anterior-posterior axis of the acquisition volume was accepted for zero degrees pitch.

Muscle	FA	ADC($10^{-3}\ mm^2/s$)	$\phi(degrees)$	$\theta(degrees)$
Genioglossus	0.282 ± 0.017	1.675 ± 0.097	20.94 ± 8.93	0
Hyoglossus	0.305 ± 0.007	1.706 ± 0.152	6.44 ± 10.26	80.18 ± 12.14
Stylo/inf.Long	0.243 ± 0.012	1.783 ± 0.100	-0.87 ± 6.93	416.59 ± 7.28

Table 4.2.1: Individual muscle mean values and standard deviations of five subjects. Fractional anisotropy, average diffusion coefficient, and average vector direction were found for the genioglossus, hyoglossus and styloglossus/inferior longitudinalis. Vector directions are described by two angles, ϕ and θ, as defined in 4.2.4.

Figure 4.2.5 depicts a midline coronal slice of the tongue obtained by DTI tractography. As shown in Figure 4.2.3 (A), the genioglossus (gg) tracts extend in a superior direction, passing between a pair of medially tilted, vertically aligned tract bundles (v). The latter tracts may be differentiated from the genioglossus tracts by the fact that they tend to curve posteriorly. A significant advantage of imaging the tongue in vivo is the ability to observe extrinsic muscle insertion angles in their resting position, for example the spiral trajectory of the stylogossus (sg) as it projects to the rear of the tongue. Shown in (B) is an oblique perspective of the same coronal imaging slice to demonstrate that, although we only observe tracts in contact with a single plane of voxels, the tracts are not contained wholly within the plane but also transect it.

We show in Figure 4.2.6 a series of 12 mm thick axial slices (superior to inferior).
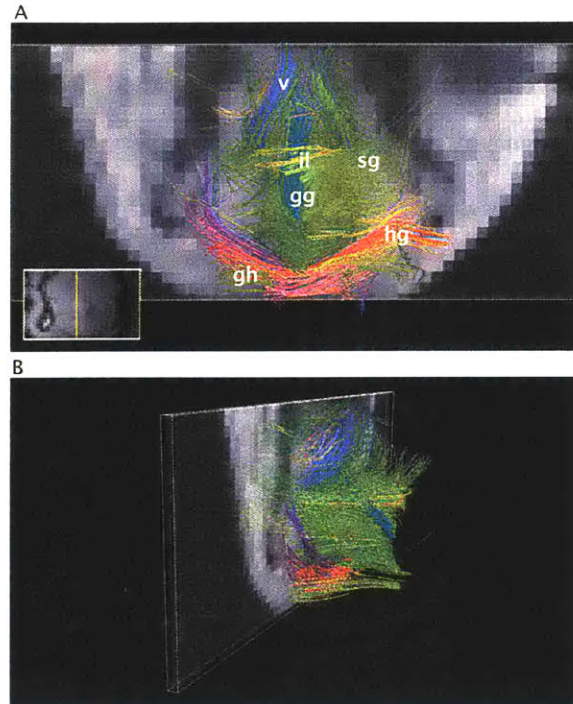
Figure 4.2.5: DTI tractography of human tongue (midline coronal). Midline coronal slice obtained by DTI tractography. (A) Coronal imaging slice shows the genioglossus tracts (gg), vertically oriented tract regions (v) and horizontal fiber tracts (il). In its natural rest position, the styloglossus (sg) follows a spiral trajectory as it projects to the rear of the tongue. (B) Oblique perspective of the same coronal imaging slice. Slice position shown in accompanying inset image. Dimensions [64,64,24], selected slice [y = 21], track length thresholds [12 mm − 140 mm].

The inset magnitude image shows the slice location in each instance in relation to the underlying anatomy. In the most superior slice (A), we observe a set of green tracts (sl), corresponding to the superior longitudinalis, which course along the dorsal surface of the tongue. This dataset is relatively sparse probably as a function of partial volume effects associated with the relatively thin muscle region. Beneath the longitudinal sheath, in the second axial slice (B), a symmetric pair of violet track groups emerges in the lateral edges of the lingual core. The most anterior portion of these tracts (v) is likely to correspond to the vertically aligned intrinsic muscles due to the fact that they originate and terminate within the lingual core. However, the more posterior of these vertically aligned tracts bundle together as they continue downwards towards the hyoid bone leading to the supposition that they correspond an extrinsic muscle. In the third axial slice (C), the spreading fan of tracts located in

the central region of the tissue corresponding to the genioglossus (gg) spreads wider in the posterior region than in the anterior region. The green longitudinal tracts confirm the presence of a thick styloglossus (sg) insertion into the tongue body that merges with the inferior longitudinalis, coursing along the lateral edges and wrapping around the anterior tip of the tongue. In the succeeding two slices, (D) and (E), a clear delineation between the genioglossus (gg) and hyoglossus (hg) is observed. Of note in the most inferior slice, (F), the tracts associated with the geniohyoid (gh) and hyoglossus (hg) appear to merge in the region of attachment to the hyoid bone.
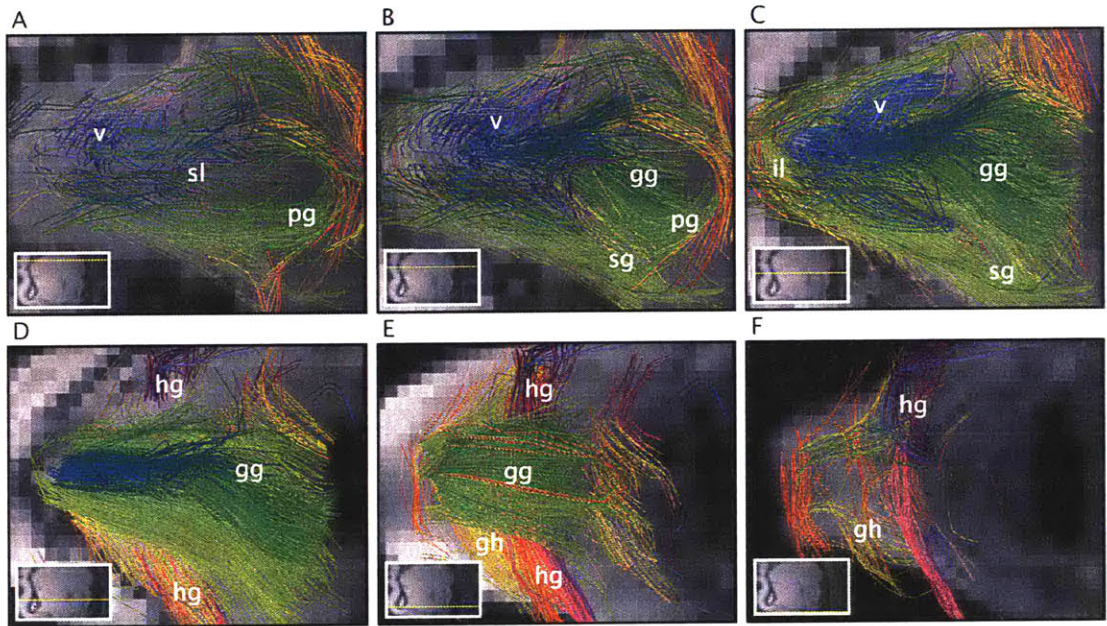
Figure 4.2.6: DTI tractography of human tongue (axial). Depicted is a set of six 12 mm thick axial slices of the human tongue obtained by in vivo DTI tractography viewed from the superior direction and arranged superior (A) to inferior (F). The superior longitudinalis (sl) blends with the palatoglossus and exit the lingual core. The symmetric pair of violet track groups (v) is likely to correspond to vertically aligned intrinsic muscles. The genioglossus (gg) spreads notably wider in the posterior region than in the anterior region forming a triangular shape bordered by the styloglossus (sg) and the inferior longitudinalis (il). In the most inferior slices, we observe the mode of attachment to the hyoid bone of the genioglossus (gg), hyoglossus (hg) and geniohyoid (gh). The slice location relative to underlying anatomy is shown by the inset magnitude in each instance. Dimensions [64.64.24], selected slices [z = 1-3, 3-7, 7-11, 11-15, 15-19 and 19-23], track length thresholds [12 mm − 140 mm].

We demonstrate in detail in Figure 4.2.7 how the symmetric pair of tract groups

originating in the lateral edges of the lingual core bundle together and pass adjacent to each other as they leave the body of the tongue. Interestingly, the tracks from the more anterior portion cross over those beginning more posteriorly before heading to their respective bony attachments. The greener tracts within the body of the tongue, which appear to represent the inferior longitudinalis (il), progressively merge with the bluer tracts of the verticalis (v) forming a continuous spectrum within the tongue but separate into distinct muscles as they exit. Previous anatomical descriptions have not made this observation. The most posterior of the verticalis (v) plunge medially of the styloglossus (sg) where, in some subjects, the fibers then merge with the hyoglossus. It is possible that these fibers correspond to the chondroglossus, an extrinsic muscle which is sometimes considered part of the hyoglossus because they possess the similar phylogenetic origin [54]. Our results do seem to show the chondroglossus to have significant differences from the hyoglossus in course and spreading manner, but because DTI cannot resolve intramuscular terminations of similarly oriented consecutive fibers we are unable to assuredly identify its presence. Finally, notice how the palatoglossus (pg) sweeps in from above where it aligns with the superior longitudinalis and ensheaths the lingual core.

4.2.3   Discussion

The determination of the extent to which myoarchitecture predicts regional mechanics for complex muscular organs provides an opportunity to explore fundamental questions relating structure and function. The tongue is a particularly interesting model of structural complexity since it is characterized by the extensive merging of intrinsic and extrinsic fibers. The intrinsic musculature of the tongue consists of a core region of orthogonally related fibers, contained within a sheath-like region of longitudinally oriented fibers. These intrinsic fibers are merged with extrinsic fibers that modify shape and position from the superior (palatoglossus), posterior (styloglossus), and inferior (hyoglossus and genioglossus) directions. The utility of diffusion based MRI for resolving structure-function relationships for the human tongue during physiological motion is based largely on its ability to resolve these intricate fiber relationships. In
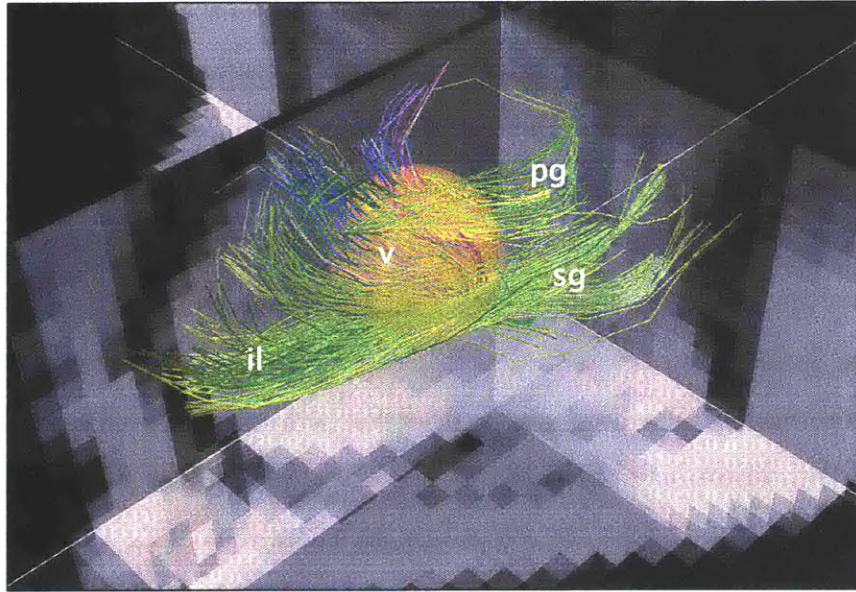
Figure 4.2.7: Demonstration of the mode of styloglossus insertion into the tongue body. Oblique orientation image of DTI tractography showing those fibers in contact with a spherical ROI (transparent orange sphere) at the point of lingual insertion of the styloglossus. The verticalis (v) fibers plunge medially of the green styloglossus (sg), though the muscles appear to form a continuous spectrum along with the inferior longitudinalis (il) in the body of the tongue. Dimensions [64,64,24], selected ROI [center at x = 37, y = 21, and z = 17, radius 4.25], track length thresholds [$15\,mm -$ $140\,mm$].

order to apply diffusion based anatomical imaging in vivo, we elected to use an approach combining multiple gradient direction DTI with tractography. While lacking the ability to resolve intravoxel crossing fibers, complete DTI tractography scans can generally be completed in a small fraction of the time required for DSI with equivalent voxel size and max b-value settings. The use of multiple gradient directions lengthens scan time, but necessarily improves SNR. Furthermore, DTI tractography should have the capacity to resolve intervoxel crossing in offset planes and non-crossing fibers at a scale that coincides with the practical dimensions of physiological shape changes, such as occur during swallowing.

The current results display for the first time the use of DTI tractography in vivo to visualize the complete structural anatomy of the human tongue. These results confirm the general conceptualization of lingual myoarchitecture as a core region of orthogonally aligned and crossing fiber populations encased within longitudinally

aligned fibers. all of which merge with externally connected extrinsic fiber populations. However. the current study also introduces the ability to observe the specific geometric relationship between the extrinsic and intrinsic muscle in the rest position. Accordingly, based on the current results, we have made the following observations:

1. The genioglossus distributes in a fanlike manner throughout the body of the tongue and merges with the intrinsic verticalis muscles in the anterior tongue. The transverse distribution of the genioglossus is notably wider in the posterior tongue as compared with the anterior tongue, suggesting perhaps a greater role in the formation of the accommodating concavity necessary for bolus formation during the swallow and for promoting lingual rotation during propulsion.

2. The prominent styloglossus fibers merge specifically with the inferior longitudinalis fibers while coursing long the lateral edges and finally encircling the anterior tip of the tongue. This suggests a very important role of the styloglossus not only for promoting gross retrograde displacement during bolus propulsion, but for controlling the more subtle variations of tongue shape needed for some aspects of early accommodation and speech.

3. The styloglossus rotates at the point of its insertion into the tongue, forming a spectrum within the tongue of variably oriented fibers involving the extrinsic fibers originating both posterior and inferior to the body of the tongue, and the longitudinally and vertically aligned intrinsic fibers. The functional implications of this relationship are not known.

The current results provide a mechanism to explicitly relate the complex myoarchitecture of the human tongue with its mechanical function. The patterns of deformation exhibited by the tongue during physiological motions such as speech or swallowing are based on its capacity to function as a muscular hydrostat, a structure defined by its ability both to create motion (via tissue displacement) and provide the skeletal support for that motion (via elongation and stiffening). Such a tissue capitalizes on its high water content. and hence incompressibility. to modify its form. A constant morphological feature of all such hydrostats in nature is the coexistence of muscle fiber populations. which are both perpendicular (transverse. vertical. circum-

ferential, or radial) and parallel (longitudinal) to the organ's long axis. The existence of merged extrinsic and intrinsic fiber populations provides a mechanism for the many possible degrees of mechanical freedom achievable by the tongue. and may represent as well an example by which biologically redundant mechanical systems are employed to ensure the performance of vital functions, such as swallowing, airway protection, and communication.

While DTI tractography possesses clear advantages for resolving tract-like structures at the current length scale in vivo, by restricting the diffusion profile to only a single maximum the tensor fitting process potentially causes artifact in tractography construction. Two distinct fiber populations intersecting at an angle within a voxel will produce a major eigenvector at an angle in-between the actual fiber orientation vectors [81]. It has been previously shown that many regions within the tongue do exhibit intravoxel orientational heterogeneity [26], and therefore directional trends shown by DTI tractography could be misrepresentations of the underlying fiber architecture. In addition, in regions where we expect fiber populations to be situated nearly perfectly orthogonally, a toggling phenomenon could result in large fluctuations in the vector field [49], thereby exceeding the angular threshold for tract connectivity. Such an effect would result in sparse and short tracts, as were evident in the anterior tongue in the current study. Several possible strategies may be used to address the limitations of DTI; for example, Q-ball imaging (QBI), a method based on the acquisition of diffusion data on a shell of constant diffusion sensitivity (single or limited number of b-values) [80]. Due to the large number of gradient directions, it is feasible to process the data acquired during this experiment using the QBI method. but the low b value may not provide enough contrast to resolve multiple maxima. While DSI is preferred to resolve fiber direction in the central nervous system due to the large variation of fiber intersection angles, the more orthogonally aligned fibers found in the tongue may allow the use of QBI. Since skeletal muscle has a diffusion constant on the order of 2 to 3 times that of white matter in the brain [67, 58]. high angular resolution methods and further reduction of voxel size [82] should be possible for imaging skeletal muscle.

In conclusion, we have demonstrated here the ability of DTI tractography to resolve the highly complex anatomical relationships existing between the intrinsic and extrinsic fibers of the human tongue in vivo. By resolving the complete 3D myoarchitecture of the human tongue. this approach should allow us to consider fundamental structure-function relationships for the tongue, as well as similar muscular organs, such as the heart and the GI tract.

4.3 Strain rate during propulsive phase of the swallow

This section describes an attempt to answer some of these questions posed in Section 4.1 regarding what muscles are involved in the series of precise and complex shape changes that occur during the swallow. It briefly covers how the local material strain rate field at a series of time points during the swallow was accomplished using phase contrast (PC) MRI and the comparison to muscle architecture (acquired as described in Section 4.2). This work was done in collaboration with Samuel Felton during completion of his masters in engineering of Biological Engineering [15].

4.3.1 Phase contrast imaging

PC MRI determines the local (single voxel) velocity function by applying a phase gradient followed by a canceling (decoding) phase gradient, then deriving local motion along the gradient vector by the phase shift exhibited by the resulting MR images [13. 63. 84]. PC MRI then uses echo planar imaging (EPI) as a fast imaging sequence to capture the data. An example of raw magnitude and phase data is displayed in Figure 4.3.1. In the top row are shown the four individual magnitude images taken with the four encoding gradients (at the same spatial resolution as the phase images below). The bottom row displays the corresponding phase images, with white representing a phase shift of $+180°$ and black representing a phase shift of $-180°$. The shading gradient is proportional to the change in strain in the direction of the

phase gradient. The tongue exhibits varying levels of phase contrast, consistent with varying strain rates, whereas the relatively small gradient within the brain indicates minimal to no strain rate. The noisy pattern around the head is indicative of random phase data and is consistent with a low signal area. It should be noted that the region of the middle tongue in which black borders on white does not indicate a steep phase gradient, but suggests that the phase has *rolled over* from $+180°$ to $-180°$ a condition assumed by the strain rate algorithm to possess the smallest possible phase difference.

During PC MRI, velocity encoding is typically applied in 4 quadrilateral directions:(x,y,z), (-x,-y,z), (x,-y,-z), (-x,y,-z) and strain rate determined by the difference in velocities between adjacent voxels distributed throughout the sampled slices of tissue. During deformation, strains near each point in the material can be linearly approximated by the strain tensor, given by a 3×3 matrix. There are several advantages to the use of phase contrast methods to assay material strain during rapid physiological motions:

1) PC MRI provides motion sensitivity that can be set to high values by adjusting the gradient pulse intensities. Thus phase contrast data have near perfect motion specificity and may be analyzed by automated schemas. Combining phase contrast with single-shot image acquisition significantly strengthens the quality, sensitivity, and specificity of phase contrast data by excluding the influence of variable motion across multishot acquisitions that otherwise would be amplified by strain calculation.

2) In contrast to tagged magnetization, PC MRI provides a basis for the acquisition and analysis of 3D strain. This, however, requires an increase in the number of strain encoding axes and thus requires slightly longer acquisition times (due to reduced sensitivity) and exhibits some algorithmic fragility. While magnetic susceptibility artifacts resulting in spatial distortions may occur during the course of oral cavity imaging due to the fact that acquisitions must be performed at air-tissue interfaces [64], these effects appear to be relatively small at the edges of the lingual tissue [21] imaged in vivo and are not detectable in the interior of the tissue [49, 50] where strain rate measures are performed. Individual phase-contrast images were

| Encoding Vectors | (1,1,1) | (1,-1,-1) | (-1,1,-1) | (-1,-1,1) |

Magnitude Images
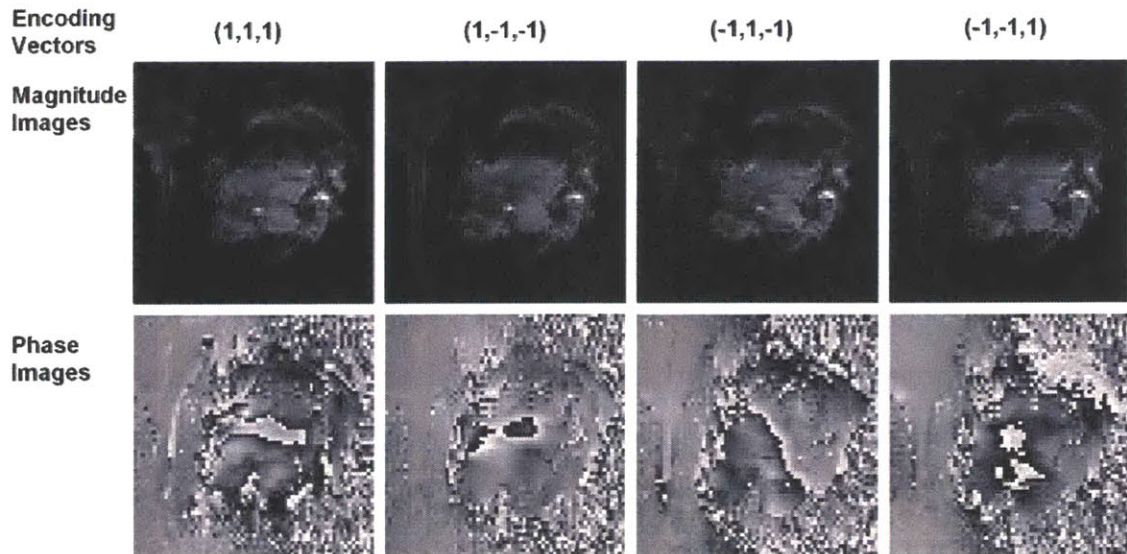
Phase Images

[ht]

Figure 4.3.1: Shown are a set of 4 magnitude (upper row) and associated 4 phase images (lower row) specific for each gradient direction in the case of a single time point (0 ms, trigger point). Each strain rate tensor image requires four scans, encoded with four different gradient vectors, embodying a magnitude image and a phase image. The four 1-D strain rate arrays are combined into one 2-D strain-rate array. Note the contrast between the high strain phase images of the tongue, characterized by gradual shade gradients, the low strain phase images of the brain, characterized by little or no shade gradients, and the low signal areas outside of the head, characterized by the random, snowy phase.

determined to have a signal-to-noise ratio (SNR) of 48.5.

Simultaneous echo refocusing (SER) PC imaging allows multiple slices to be imaged simultaneously by sampling voxels from alternating slices. In normal MR images, the imaged plane is chosen by a single-slice selective RF pulse. SER uses a sequence of selective RF pulses, separated by defocusing pulses so that each slice has a different phase history. In this way the data is multiplexed. The signal from the different slices are refocused simultaneously, to reduce the gradient duty cycle and dead time.

4.3.2 Physiological Gating of MR Imaging

Given the spatial and temporal complexity of the mechanical events associated with swallowing and the one-dimensional nature of conventional phase contrast data, gating is needed to temporally align the resulting mechanical information. While supe-

rior temporal precision would result from cine MR image acquisition [72], obtaining multiple phase contrast MR images following a single gating pulse was not feasible. Owing to the fact that propulsion is principally reflexive once initiated we elected to tether MR image acquisition to lingual pressure applied to the hard palate through a pressure-sending bulb at the approximate outset of the propulsive phase [51, 68]. The device configuration is portrayed in 4.3.2. A small (3 cm length) tongue bulb (Iowa Oral Performance Instrument, [35] Blaise Medical) was placed immediately behind the front teeth and on the tip of the subject's tongue. The bulb was connected via 15 m of 1/16" ID tubing to a pressure sensor, from which output was acquired and analyzed by Labview software. The peak pressure occurring secondary to tongue pressure against the bulb was recorded and a 5 V output signal triggered when a threshold pressure (approximately 0.35 PSI) was achieved. Acknowledging that there is likely to be variation between subjects in the pressure applied by the tongue during swallow initiation, the exact pressure threshold was derived for each subject by determining the voltage threshold immediately preceding the swallow in 4-8 test swallows, then setting the voltage threshold to 0.01 V below the smallest peak achieved in the test swallows. While the interval between the time of initial tongue contact with the sensor and the achievement of threshold pressure varied slightly between subjects, the interval between the time at which threshold pressure was obtained and the initiation of lingual displacement (and the coordinated initiation of MR scanning) was < 0.1 second and highly reproducible. It is conceivable that the presence of the bulb in the oral cavity may cause a deviation from the natural positioning of the tongue, and thus induce compensatory mechanical actions. In addition, the resistance provided by the bulb may modify the natural strain patterns exhibited by the tissue during the course of swallowing. While in preliminary experiments, the bulb was easily positioned by subjects by placing one edge of the bulb against the teeth resulting in tongue tip displacement, there was a small amount of accommodative lingual deformation and superior hyoid displacement as a function of bulb positioning in the anterior oral cavity (Figure 4.3.2C). The effect of this pre-swallow accommodative effect could not be systematically assessed in the current protocol since the presence of the intra-oral

device was essential to the acquisition of MR data.
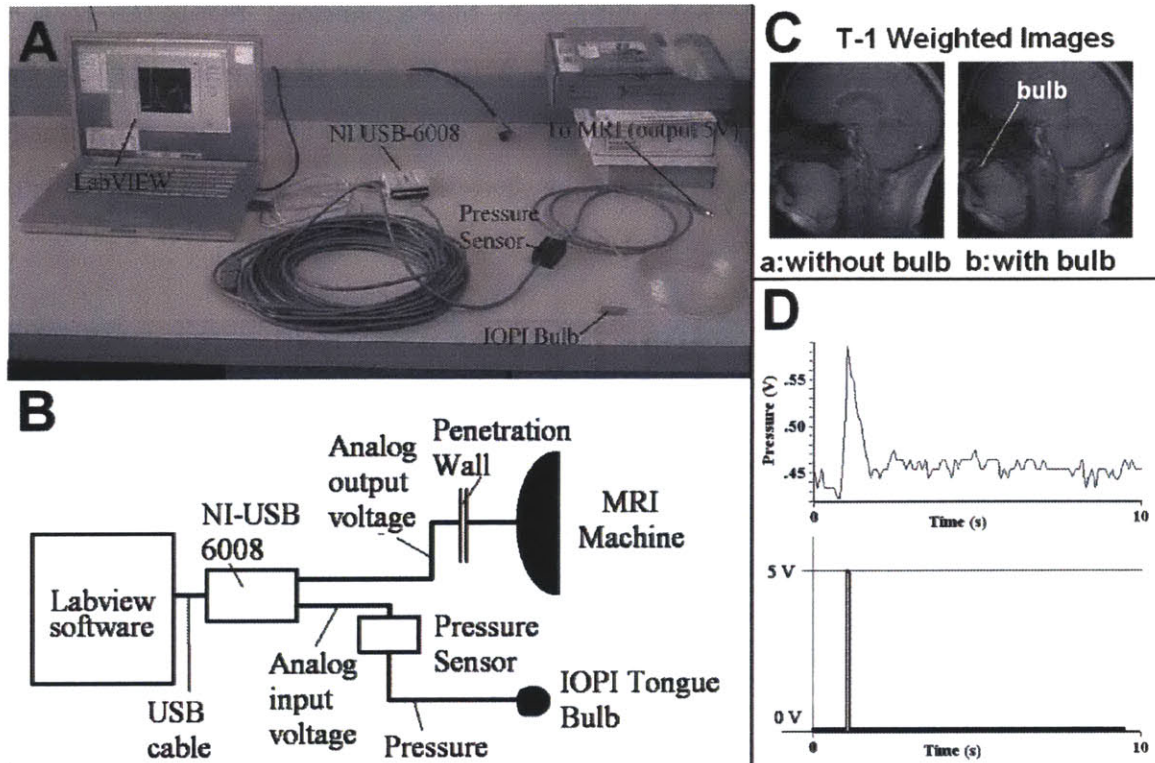
Figure 4.3.2: A swallow based MR acquisition gating system was developed to provide a basis for precise temporal sequencing and spatial registration, based on the pressure applied by the tongue to a sensing bulb (Blaise Medical) situated against the hard palate at the outset of late accommodation. Upon achieving threshold pressure, a $5\,V$ signal is elicited which triggers MR acquisition. A) Photograph of system components, consisting of a small ($3\,cm$ length) tongue bulb in series via 1/16" ID tubing with a pressure transducer whose output is directed to Labview hardware/software and a pressure driven $5\,V$ trigger signal elicited. B) Block diagram of system components. C) Magnitude MR images of the tongue in the absence of (a) and the presence of the gating bulb (b) indicating accommodative lingual deformation and hyoid displacement as a function of bulb position. D) Pressure tracing (upper) induced by the tongue applied to the hard palate via the sensing bulb and the threshold for eliciting an electrical trigger pulse (lower tracing).

4.3.3 Results

Two-dimensional diffusion vectors were measured via DTI MRI and connected into mesoscale structures via tractography. These tracts represent the mid-sagittal fiber architecture of the tongue. The color and shade of these tracts represents the direction

of and magnitude of the strain rate eigenvector and the amount of alignment with the co-located diffusion vectors (red compression, blue expansion). Strain rate tensors were derived in a sagittal image slice using PC MRI for a set of voxels comprising the tongue during the propulsive phase of swallowing of a 3 ml water bolus. Each image was compiled by averaging two simultaneous slices, comprising five sets of strain rate data each, acquired from 20 swallows total.
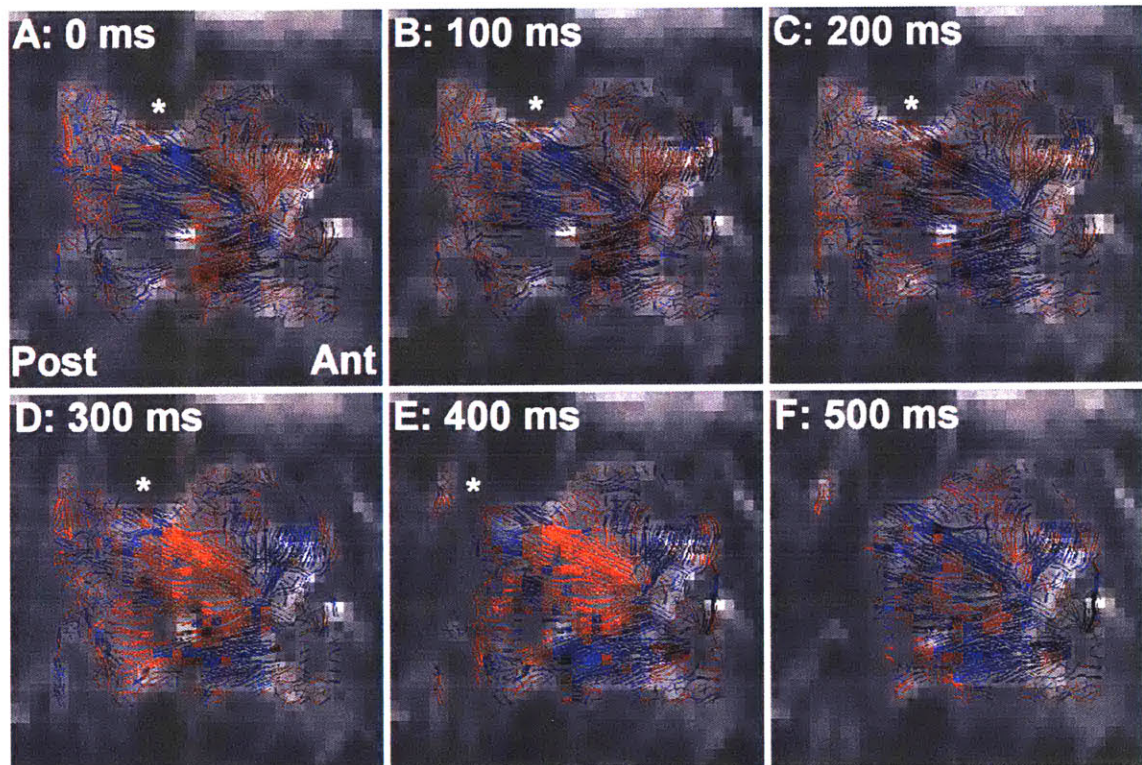
Figure 4.3.3: Two-dimensional mid sagittal myoarchitecture of the tongue was derived with DTI and connected into mesoscale structures via tractography. The color and shade of these tracts represents the direction and magnitude of the dot product of the strain rate eigenvector with the co-located unit diffusion eigenvector. Strain rate tensors were derived in a sagittal image slice using PC MRI for a set of voxels comprising the tongue during the propulsive phase of swallowing of a $3\,ml$ water bolus (red compression, blue expansion).

In 4.3.3 two-dimensional tractography for one subject is shown at $0\,ms - 500\,ms$ after the gating signal. At $0\,ms$ (A), compression can be seen in the fibers representing the verticalis and the palatoglossus, as well as expansion in the genioglossus. This expansion could be due to the contraction of the styloglossus in the superior-posterior

of the tongue, pulling on the genioglossus, or orthogonal expansion related to contraction of the palatoglossus. 100 (B) and 200 ms (C) show similar strain rate events, but in slowly decreasing magnitude. At 300 ms (D) compression in the palatoglossus continues. Compression also occurs throughout the genioglossus and expansion in the geniohyoid and verticalis, likely relaxation of contraction. 400 ms (E) shows continued compression in the genioglossus and expansion in the genioyoid and verticalis, as well as a bulk longitudinal shortening of the tongue, as the bolus opens into the throat. 500 ms (F) shows expansion throughout the tracts, along with isolated voxels of compression in the verticalis and the genioglossus.

4.3.4   Discussion

Through the application of gated phase contrast MRI, we studied the mechanisms involved in the genesis of rapid lingual reconfiguration during propulsion. Our current results demonstrate that: the propulsive phase of swallowing is associated with a tightly organized series of compressive and expansive events occurring within a period of approximately 600 ms. In the initial portion of the propulsive phase (images obtained at the time of gating pulse application and 200 ms from the gating pulse). we observed the following events: 1) obliquely aligned compressive and expansive strain in the approximate fan-like distribution of the genioglossus, 2) vertically aligned compressive strain consistent with passive compression secondary to palatoglossus contraction and active compression secondary to verticalis contractions combined with orthogonal expansion, 3) compressive strain aligned obliquely between the anterior-superior to the posterior-inferior regions with commensurate expansion in the posterior superior region, effects possibly related to passive compression due to laterally inserted contraction of the hyoglossus, and 4) compressive strain aligned obliquely and directed to the styloid process. The latter may reflect passive compression due to the laterally inserted fibers of the styloglossus or active compression secondary to more medially inserted fibers. The combined effect of these mechanical events is the effective re-configuration of the tongue prior to posterior displacement. Lingual deformation during the latter portion of the propulsive phase (images ob-

tained at 400 and 600 *ms* from the gating pulse) appeared to involve prominent compressive strain occurring in the mid and posterior region of the tissue obliquely aligned between the anterior inferior and posterior superior regions of the tissue, suggestive as well of the distribution of the genioglossus with commensurate orthogonal expansion, along with bidirectional contraction in the approximate distribution of the intrinsic core fibers and expansion in the anterior-posterior orientation. Interestingly, this expansive phase coincided precisely with the delivery of the flattening of bolus-containing concavity and the apparent delivery of the bolus to the pharynx. Despite some intersubject variation in the precise timing of compressive and expansive strain rates, these general patterns were exhibited by all subjects, thus substantiating the postulate that the cardinal lingual motions are a due to mechanical interactions of the intrinsic and extrinsic muscles.

This approach constitutes a significant advance over previous techniques since it provides a method to assay simultaneously the rates of compression and expansion during physiological motion. This technique may potentially be combined with measures of underlying lingual myoarchitecture, thus constituting a method by which the rate and direction of fiber shortening can be determined. We previously considered the proposition that propulsive lingual deformation is associated with a combination of internal stiffening and hydrostatic elongation resulting from the bidirectional contraction of the transversus and verticalis muscles combined with retracting force applied by the laterally inserted styloglossus [49]. We have now extended this conceptualization of tongue deformation to include a more complex sequence of material strains (compression and expansion) involving the various segments of the genioglossus muscle. tight integration of extrinsic and intrinsic strain behavior, and passive elements of compressive and expansive strain related to contractions not included in the particular imaging slice i.e. styloglossus and hyoglossus, and secondary mechanical events imposed by the tongue's inherently isovolemic conditions. It should be recognized that the exact timing of the events described may vary somewhat with prior descriptions of lingual deformation due to the presence of the bulb in the oral cavity and changes in lingual shape and mechanics before the initiation of the observed

sequence.

The extension of phase contrast MRI, previously applied to determine cardiac strain, to imaging the mechanical function of the tongue during swallowing contained several technical challenges, owing to the fact that the tongue is both structurally and mechanically more complex than the heart. By establishing a method of MRI gating associated with threshold lingual pressure applied to the hard palate during late accommodation, and by adopting a velocity encoding for the highly variable strain rates exhibited by the tongue with minimal artifact attributable to the air-tissue interface in the oral cavity, we were able to achieve reliable strain rates involving the tongue during swallowing. However, several limitations of this approach should be acknowledged. While generally consistent mechanical patterns were exhibited, some of the events shown were quite variable. By our analysis of this variability, it may be that precise times where certain mechanical events occurred varied subtly but significantly between subjects, an issue which could become even more important in the case of pathological tongue motion. We anticipate accordingly that future studies may thus require considerably greater temporal resolution. A second limitation was the need to resolve transverse planar strain separate from anterior-posterior planar strain. While the high degree of mechanical symmetry and coherent strain rate patterns exhibited by the tongue indicate that we are accurately measuring strain rate in the tongue, there are theoretical limitations for resolving complex intravoxel strain patterns, which would be helped through the use of techniques capable of acquiring 3D strain rate directly. We should also acknowledge that since our current approach is directed to resolving internal tissue strains, it does not have sufficient resolution to accurately determine surface deformation or possess appropriate contrast to visualize bolus displacement [2, 7, 57, 89]. Thus the relationship between internal strain and physiological bolus manipulation can not be measured directly with the current techniques.

We conclude that gated phase contrast magnetic resonance imaging can be adapted with appropriate gating to assay the tongue's internal strain events associated with bolus propulsion. Our results demonstrate that bolus propulsion may be attributed

to a synergistic sequence of compressive and expansive mechanical events involving both the intrinsic and extrinsic muscles, whose net effect is the orderly delivery of the ingested bolus from the oral cavity to the pharynx.

Chapter 5

Ex vivo: esophagus and heart

In this chapter, DW-MRI is applied to the study of ex vivo specimens. The results revealed several unique aspects of the cardiac and esophageal myoarchitecture.

5.1 Myoarchitecture of the normal and infarcted sheep heart

The unique functional capacity of the heart depends critically on the organization of cardiac muscle fibers in layers of counter-wound helices encircling the ventricular cavity. This pattern allows a special twisting motion during systole and early diastole, which is essential to the mechanical efficiency of the normal ventricle to eject and suction venous return. It is our intention to delineate the quantitative geometry organization of the intact heart for the future employment of finite element simulations. The use of these models will be instrumental in understanding both normal and pathological function of the heart, and therefore for predicting the therapeutic response of various therapeutic drugs and devices. In this chapter, we look briefly at preliminary data the sheep heart and consider the structure in terms of proposed unified models.

5.1.1 Methods

Sheep hearts (normal n=2, infarcted n=1) obtained through a collaboration with the University of Maryland were imaged with diffusion spectrum imaging. Acquisitions were performed at $4.7\,T$ with a max b-value of $16,000\,s/mm$, $1\,mm^3$ isotropic voxels, $1300\,ms$TR and a $128 \times 128 \times 128$ matrix size.

5.1.2 Normal cardiac myoarchitecture

The normal mammalian heart has been observed to exhibit a gradation from left-handed helical fiber orientation in the epicardium to right-handed endocardium [73]. The DSI tractography data obtain confirms this observation for the left ventrical as well as the right ventrical; though, the right ventricular is much smaller, not circular, and has a much thinner wall. The graded transition through the midventricular septum allows both ventricals to have right-handed endocardiums and left-handed epicardiums (Figure 5.1.1B).

Based on our initial observations, we theorize that the heart may be considered as a unique structure termed a double toroidal helix. One toroidal helix encircles the entire heart (Figure 5.1.1C) while a smaller helix lies within the first, sharing part of the left ventricular wall. The right ventricle appears as an extension of the left ventricle. Because both ventricles share a common wall as part of the interventricular septum, the function of both ventricles must be fundamentally connected. Toroidal space is the name used to describe the area and volume of a torus or so-called doughnut shape. The implications for analysis of structures in terms of its toroidal properties are great, and relevance may be gained in relation to the studies of physics (and metaphysics), astronomy, and energy systems. To our knowledge the explicit analysis of biological mechanics in terms of toroidal helical properties is novel.

Relatively recently, a unified model of the heart has been developed called the Torrent-Guasp helical ventricular myocardial band [75]. The model describes the overall heart myoarchitecture by a single band starting at the pulmonary artery (PA), looping around both ventricals and ending at the aorta (AO). We display in Figure
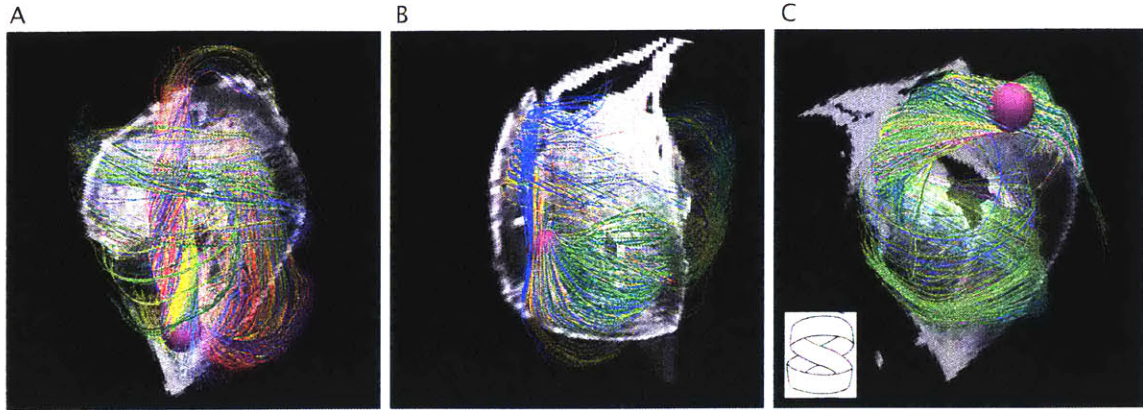
Figure 5.1.1: DSI tractography of sheep heart myoarchitecture. (A) Shows the twisting appearance of fibers descending from a papillary muscle and their divergent course to the outer walls of both ventricals. (B) ROI placed in the mid-ventricular septum showing the fan-like form of the gradual helix angle transition between right-handed endocardial surfaces of each ventrical. (C) Selection of tracts which resemble the toroidal helix form (inset).

5.1.2A how a particular set of tracts selected with an ROI do follow a trajectory that closely resembles the Torrent-Guasp model (B). Of particular interest is the region of beginning/ending at the PA/AO (C). DSI tractography shows some tracts continuing through this junction, though the continuity may simply be an artifact of the tractography method for which the *jumping* from one streamline to a neighboring steamline is possible.

The reason for the heart's complex architecture is not thoroughly understood. One explanation that has been proposed is that the helix configuration leads to most shear strain occuring in cleavage planes between transverse laminae, thereby allowing maximal wall thickening during systolic contraction [41]. A second explanation is that complex architecture is necessary for relaxation, or diastole [1]. It is known that hearts will continue to pump blood even if the blood pressure is equal to atmospheric, therefore the heart must have means to create negative pressure. The stored torsional strain from contraction can supply the necessary energy for suction of blood to refill the ventrical.
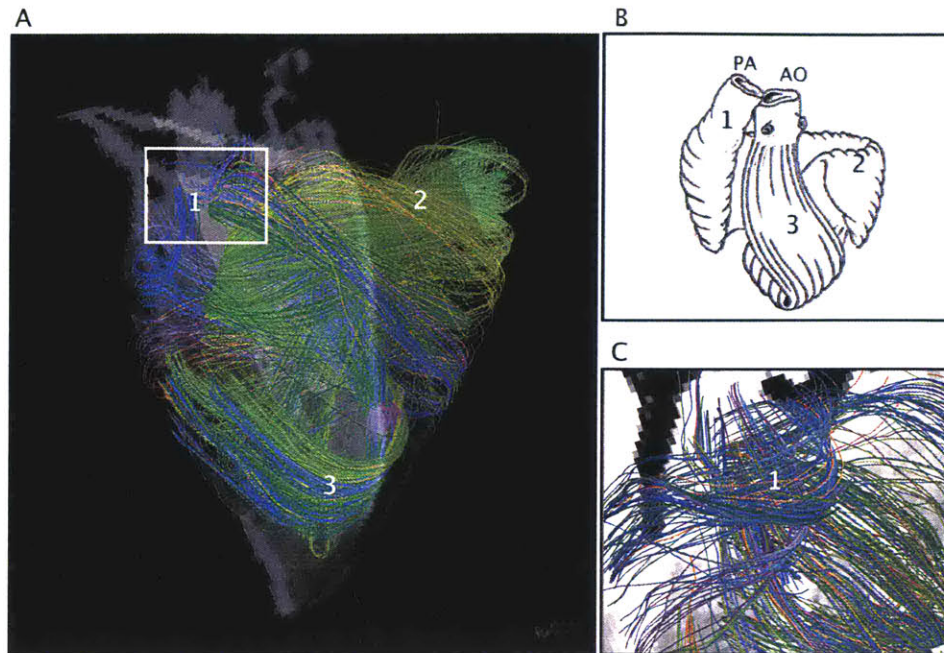
Figure 5.1.2: Helical ventricular band model of sheep heart myoarchitecture. Image of DSI tractography of normal sheep heart (ventral orientation) (A) Diagram of Torrent-Guasp helical ventricular myocardial band obtained from Torrent-Guasp, 2005 [75] (B). Close-up of region of pulmonary artery (PA) and aorta (AO) (white square in (A)).

5.1.3   Remodelling following infarction

Following myocardial infarction, the process or remodeling includes: death and thinning of ischemic zone, hypertrophy and reduced contractility of non-ischemic tissue, and progressive left ventricular dilation and wall thickening. Remodeling can either be adaptive (benificial) or maladaptive (progressively leading to worse heart function and heart failure).

Preliminary data was acquired for an infarcted sheep heart and is shown in comparison to a normal sheep heart in Figure 5.1.3. The infarcted sheep heart shows the expected wall thickening except for the ischemic zone. Additionally a general disarray in fiber alignment is noticeable compared to the normal organization. In the region of infarct (marked by the white arrow) only epicardial and endocardial tracks appear. which may be due to the fact that only these cells survive due to their being supplied blood by surface perfusion.
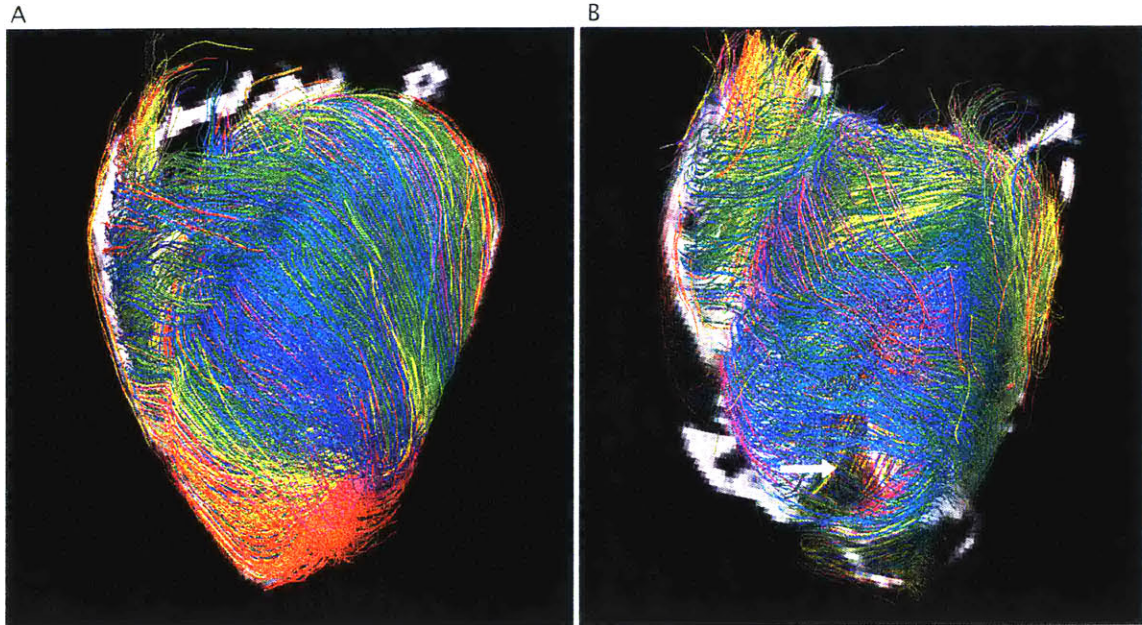
Figure 5.1.3: DSI tractography of normal and remodelled cardiac myoarchitecture. Normal sheep heart (ventral orientation) (A), and sheep heart approximately 15 days following infarction (ventral orientation) (B), showing general disarray in fiber alignment and thinning with only endocardial and epicardial tracks discernible in region of infarct (white arrow).

5.2 Myoarchitecture of the bovine esophageal wall

Here, we propose a new understanding of the muscular anatomy of the mammalian esophagus. We imaged its myoarchitecture with diffusion spectrum magnetic resonance imaging (DSI) and tractography. We demonstrate that the proximal body of the esophagus consists of helically aligned crossing fiber populations, which overlap between layers in the form of a zipper region along the length of the tissue. With increasingly distal position along the length of the tissue, helix angle and skeletal muscle prevalence are reduced such that fibers align themselves in the most distal location into distinct inner circular and outer longitudinal smooth muscle layers. We conclude that esophageal myoanatomy consists of crossing myofibers exhibiting a decreasing degree of helicity as a function of axial position, and propose that this unique geometric construct provides a mechanism to resist distension and promote aboral flow.

Esophageal peristalsis occurring in mammalian species results from a tightly integrated aboral sequence of contractile activity involving skeletal (proximal esophagus) and smooth muscle (distal esophagus) [11]. As is the case with all muscular tissues, the mechanical properties of the esophageal wall are dictated by the distribution and orientation of its constituting fibers [17]. However, defining this relationship in the case of the esophagus is particularly difficult owing to the fact that esophageal muscle fibers are characteristically aligned along multiple spatial axes. Deriving the anatomical correlates of distensibility and contractility in the case of intact esophageal tissue thus requires a method for resolving rather complex arrays of myofibers at spatial scales at least an order or magnitude larger than conventional light microscopy.

NMR imaging of proton diffusivity partially addresses this problem by its ability to derive multiscalar 3D-resolved myoarchitecture in whole tissue [76, 70, 4]. By this method, 3D diffusivity is depicted by a probability density function related by the Fourier transform to orientation-specific attenuation of the diffusion signal (Q-space imaging) [9, 6]. In diffusion spectrum imaging (DSI), the displacement of proton spins is measured in response to a large array of gradient directions and intensities and the resulting displacement profile depicted as a 3D contour reflecting the orientation of all of the principal fiber populations per voxel [85, 42, 22]. Tractography depicts the orientation of these fiber populations across multiple voxels [3, 66] and thus generates mesoscopically resolved myofiber tracts [24, 18] believed to be comprise a structural template for local contractility. We have employed these imaging techniques here to demonstrate a previously unknown geometric relationship in tubular tissue considered to underlie the structural integration of the heterogeneously aligned musculature of the mammalian esophagus.

5.2.1 Methods

Magnetic resonance image acquisition was performed on 4 ex-vivo cow esophagi obtained from Blood Farms (West Groton, MA). Whole specimens were refrigerated and scanned within 24 hours of harvest. Data was acquired with a Siemens Allegra $3\,T$ scanner. The imaging protocol employed key-hole Cartesian diffusion gradient

sampling scheme within a sphere in q-space for a total of 515 sampling points. The maximum b-values used were in the range of $5500 - 8500\ s/mm^2$ and the voxel size was $500\ \mu m^3$.

For histological examination, sections of esophagus were fixed at least 24 hours in neutral buffered formalin, sectioned in one of more of the orientations described below, and embedded in paraffin using standard methods. Five micron thick sections were stained with hematoxylin and eosin (H and E) and examined by one of the authors (J.G.)

1. Axial sections. The esophagus was serially sectioned perpendicular to the long axis of the esophagus, producing a series of donuts from the mid esophagus to the gastroesophageal junction. These sections were examined for the composition of the circumferential muscle layers and for the orientation of fibers with respect to the transverse axis of the esophagus. That is, fibers that run in the plane of this section are oriented horizontally, those perpendicular to the plane are oriented vertically, and those oriented obliquely are helical.

2. Circumferential sections. A segment of esophagus was opened along its longitudinal axis, laid flat and serially sectioned perpendicular to the mucosal surface. Therefore, each section was oriented in a radial direction with respect to the inner lumen. The sections were examined for the orientation of fibers with respect to the long axis of the esophagus. That is, fibers that run in the plane of this section are oriented vertically, those perpendicular to the plane are oriented horizontally, and those oriented obliquely are helical.

3. Radial (or en face) sections. A segment of esophagus (including the distal half and gastroesophageal junction) obtained fresh was opened along the longitudinal axis, cut into 2 cm circumferential segments, and fixed as flat sections in plastic holders. The sections were embedded flat and serially sectioned at a total of five levels, extending from the mucosa/submucosa to the adventitia. Therefore, the plane of each section was parallel to the mucosal surface.

5.2.2 Results

We demonstrate in Figure 5.2.1A the principal direction(s) of the local diffusion maxima and their associated orientation distribution functions (ODFs) for a single axial slice derived from the mid-portion of an excised bovine esophagus. These images illustrate that the esophageal wall consists of regions in which the muscle fibers/voxel have a single fiber direction, i.e. one diffusion maximum, and regions in which there are multiple fiber directions, i.e. more than one diffusion maximum. We demonstrate in Figure 5.2.1B the construction of the tissues myofibers tracts from the principal fiber directions displayed per voxel. Extending this methodology to include the entire esophagus, we show in Figure 5.2.2 that the proximal esophagus consists characteristically of helically aligned crossing fiber populations, with gradual variation of helix angle as a function of position along its length. The fibers were color-coded according to the helix angle with respect to the central axis, with mean local helix angles ranging from 60° to near horizontal. The fact that a distinct longitudinal layer is not observed in the proximal esophagus suggests that both the outer and inner muscular layers exhibit similar helicity. However, with increasingly distal position, the fibers align themselves into distinct inner circular and outer longitudinal muscle layers. The longitudinally aligned fibers are configured as bands of fibers in the outer layer of the distal esophagus, and extend from the distal esophagus across the EG junction into the proximal stomach.

Considering the relationship of the right and left handed helices in more detail, the intersection of these myofiber tracts appears to exhibit a unique interweaving of inner and outer tract layers along a zipper region (Figure 5.2.3). The variation of helix angle associated with this zipper configuration was expressed as a histogram where the number of tracts exhibiting a specific through-plane angle is shown. By ascertaining tracts directly, as opposed to counting vectors of in-plane voxels, multi-voxel trends are provided more weight. These data demonstrate a gradation of helix angles for the constituting myofibers as a function of axial position, ranging from 60° in the proximal esophagus (corresponding to tissue with a predominance of skeletal muscle)

to near zero in the distal esophagus (corresponding to tissue with a predominance of smooth muscle). A few tracts in the outer wall increase in helix angle to form the relatively very thin longitudinally oriented layer surrounding the circumferential layer of the distal esophagus. At the esophago-gastric junction. the myofiber tracts become more completely circumferential as the tract region thickens and merges with the obliquely aligned sling fibers of the proximal stomach, resulting in a dense band of fibers aligned at approximately 30° to the axis.

In order to identify the microscopic basis for the observed myoarchitecture. detailed histology was performed in sections excised from the sections of the MRI-imaged esophagus. fixed. embedded. and stained following the completion of each MRI experiment. and displayed as sections in the axial. radial. and en face directions. Fiber bundles which are in plane with the section are typically elongated. those which are exactly cross planar are circular. and those which are at an angle to the section exhibit an ovoid shape of varying lengths. For conciseness and clarity, the planar sections are called by the direction orthogonal to the plane of section(i.e. circumferential orientation refers to those sections cut perpendicular to the circumference). Figure 5.2.4 (circumferential orientation) demonstrates in the proximal esophagus skeletal fiber bundles that are principally perpendicular to the plane of the section. In the middle esophagus, we observe several populations of skeletal muscle fiber bundles. based on orientation, juxtaposed with relatively uniformly oriented smooth muscle regions. In the distal esophagus. More limited skeletal muscle bundles are observed perpendicular to the plane of the section relative to the predominant sheets of smooth muscle. Figure 5.2.5 shows (radial orientation) more precisely the in plane relationships of the skeletal and smooth muscle cells. when the plane of reference is the circumferential layer (parallel to the mucosa) of the tissue. Most significantly. we observe the varying angular relationships exhibited by the skeletal and smooth muscle. as a function of location in the proximal. middle and distal esophagus. The fact that skeletal muscle bundles exist adjacent to each other in multiple fiber orientations relative to the plane of the section (based on the shape of the muscle bundles) indicates that the muscles bundles are likely to be interwoven across the plane of the section.

5.2.3 Discussion

Employing DSI tractography to image the excised bovine esophagus, we demonstrate that that the muscular organization of the mammalian esophagus consists not of homogeneously configured circular and longitudinal muscle fibers but by a set of helically oriented skeletal crossing muscle fiber tracts in the proximal esophagus (inner and outer muscular layers) merging gradually into distinct circularly and longitudinally oriented smooth muscle fiber tracts in the distal esophagus. The presence of crossed cylinders in the proximal esophagus is a unique mechanical construct which permits the integration of muscle components of opposite helicity and equal radius, and which is likely to result in enhanced radially aligned material strength.

It has been generally accepted that the muscular wall of the esophagus is composed of two orthogonal tissue planes, and external longitudinally aligned set of muscle fibers and an internal circumferentially aligned set of muscle fibers. The longitudinal fibers are arranged in the proximal esophagus as three fasciculi, one anterior fiber group, which is attached to the cricoid cartilage, and two lateral fiber groups, which are continuous with the muscular fibers of the pharynx. These fasciculi merge and thus form a thin outer covering to the esophagus. The circularly oriented fibers are continuous with the inferior pharyngeal constrictor, and continuous in its orientation to the esophago-gastric junction. It is further presumed that the near seamless transition from skeletal to smooth musculature contributes substantially to an uninterrupted sequence of aborally directed peristaltic contractions. The identification of a novel pattern of locally aligned myofiber populations by DSI with tractography allows us to reconsider esophageal muscular anatomy as a set of heterogeneously aligned and macroscopically resolved myofiber tracts, whose interactions provide the structural basis by which proximal skeletal muscle fibers merge over the length of the tissue with distal smooth muscle fibers. The proximal bovine esophagus, consisting principally of skeletal muscle, exhibits helix crossing at approximately 60° whereas the more distal segments of the esophagus, consisting increasingly of smooth muscle, and exhibit progressively smaller angles of helix crossing angles. At the region immediately

orad of the esophago-gastric junction (EGJ), the circumferential fibers are virtually circular, i.e. helix angle near zero. These results assume that the local diffusivity for skeletal and smooth muscle is similar as is wall thickness, such that the changes in helix angle are attributable only to anatomical variations and not partial volume effects. It should be noted that the current results reflect only the inner circumferentially aligned fiber populations, since the longitudinal layer is too thin to be visualized under the current imaging conditions.

The presence of crossing helices in the wall of the esophagus suggests a mechanism for resisting distension (i.e. stiffness) due to intraluminal stress. Variable stiffness of the esophagus may in turn relate to differences by which propulsive force is applied to a bolus, and thus the efficiency of swallowing. Based on established concepts relating helicity with tensile strength in tube like structures, we may consider a model in which the varying helix angles exhibited by the esophageal muscularis translate into differences of tissue distensibility. The general relationship between the helix angles exhibited by braided structures and tube distensibility following the application of intraluminal pressure have been described. In the current instance, we theorize that helix angle has a predictable inverse relationship with tubular distensibility. This formulation allows us to deduce the relationship between helix angle and stiffness for a segment of esophageal tissue, based on the force needed to distend the tissue to a given circumference. We speculate from this preliminary model that graded reductions of helix angle (high proximally, low distally) correlates with a graded reduction of tissue stiffness, with maximal stiffness (minimum distensibility) in the proximal esophagus, and minimum stiffness (maximum distensibility) in the region just proximal to the esophago-gastric junction. Such differences in tissue stiffness could have teleological advantages for bolus propulsion in that more rapid clearance would be expected in the proximal (less distensible) segment of the esophagus and slower clearance would be expected in the distal (more distensible) segment of the esophagus. Previous computational [53, 55] and experimental [88, 14, 74, 52] analyses of esophageal wall mechanics have focused on the relationship between applied stress and tissue distensibility (strain), and generally assumed an explicitly orthogonal relationship between

the outer and inner musculature. The generalization of our findings throughout mammalia may allow a broad reconsideration of the way in which intraluminal mechanical stress affects tissue distensibility in tubular organs and the generation of local force.

DSI tractography comprises a novel method for considering complex tissue myoarchitecture which depicts muscular organization, not as a compilation of individual myofibers, but as a set of mesoscopically resolved myofiber tracts. We propose that these mesoscale myofiber tracts constitute a structural template, which dictates the direction of local tissue shortening during deformation. We note however several limitations of this technique in regard to predicting physiological patterns of contractility. First, since DSI resolves fiber orientation through the determination of principal directions of diffusion, a certain extent of microscopic complexity obtainable by conventional light microscopy may be missed. Whether this level of resolution is significant in terms of understanding tissue mechanics has not been determined. Second, it is uncertain whether DSI tractography, at the level of angular resolution shown in this report, will be feasible in vivo due the required imaging time and the deleterious effects of gross motion. An alternative approach may be used to derive intervoxel tracts based on voxel-specific principal fiber direction with high resolution DTI [81, 18] although intravoxel crossing fibers may not be clearly resolved with this technique. While we predict that similar myoarchitectural patterns will be shown by the human esophagus, differences in muscle fiber types may be associated with differences in the orientation and distribution of helix angles for the derived fiber tracts, and consequently differences in distensibility and transit time.

We conclude that esophageal myoanatomy consists of crossing myofibers exhibiting a decreasing degree of helicity as a function of axial position, and propose that this unique geometric construct provides a mechanism to resist distension and promote aboral flow.
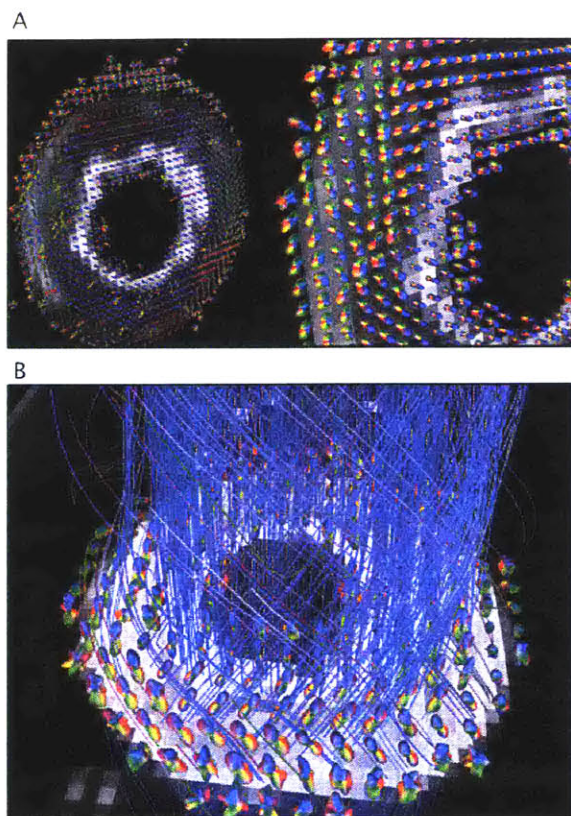
Figure 5.2.1: DSI of cow esophagus (axial view). Diffusion weighted images were acquired for a sphere of q vectors with indexed values in a Cartesian grid in q-space to produce a 3D probability distribution function. Since the 3D PDF represents a spatial volume, its dimensions may be reduced by radially integrating the PDF resulting in a distribution that is a function of fiber angle, termed the orientational distribution function (ODF). (A) Shown on the left are the vectors associated with maximum diffusion for each voxel shown, indicative of the principal fiber direction, and on the right, the ODF distribution. (B) Intervoxel connections were constructed by defining similarity of vector direction (based on the local diffusion maxima for the ODF) through the application of a streamline algorithm with an angular threshold. In this image, a set of ODFs have been constructed in an axial orientation slice and the tracts derived from the respective principal fiber directions.
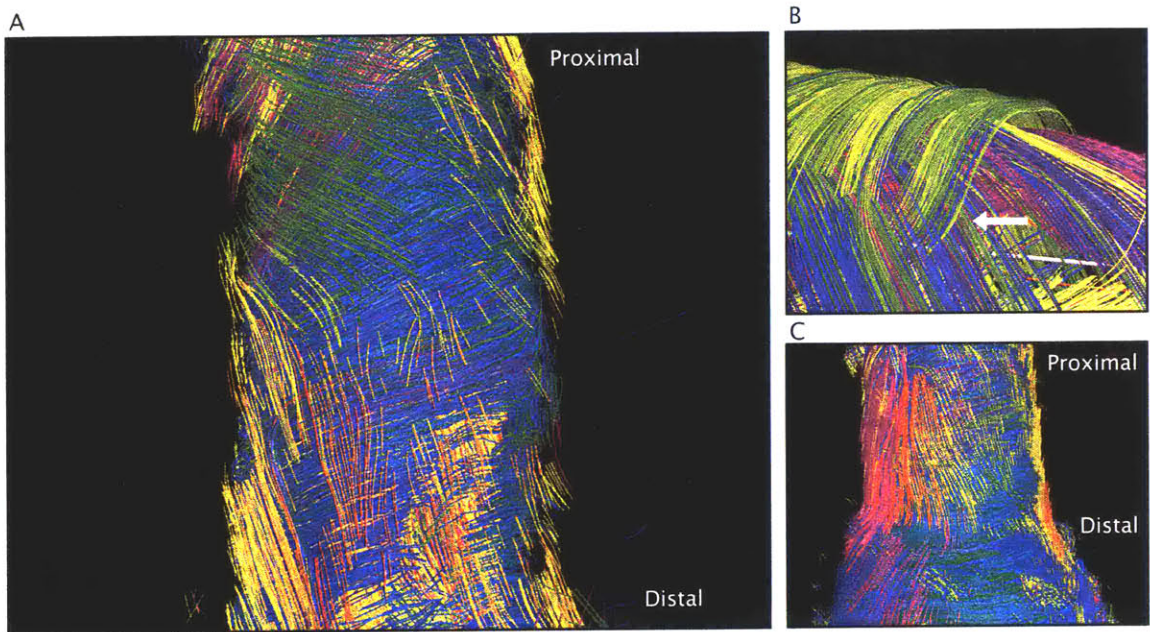
Figure 5.2.2: DSI tractography demonstrating the 3D myoarchitecture of the esophagus. DSI with tractography was employed to image the mesoscopic fiber tract structure of the intact excised bovine esophagus. Fibers were color-coded according to the helix angle with respect to the central axis. (A) View of the mid-esophagus, focusing on the transition from helical to circumferentially aligned fiber tracts with increasingly distal locations. (B) Close-up view of the proximal esophagus showing the interwoven nature of the helically aligned tracts (white arrow). (C) The distal end of the esophagus is mainly circumferential with a thin superficial layer of longitudinally aligned tracts.
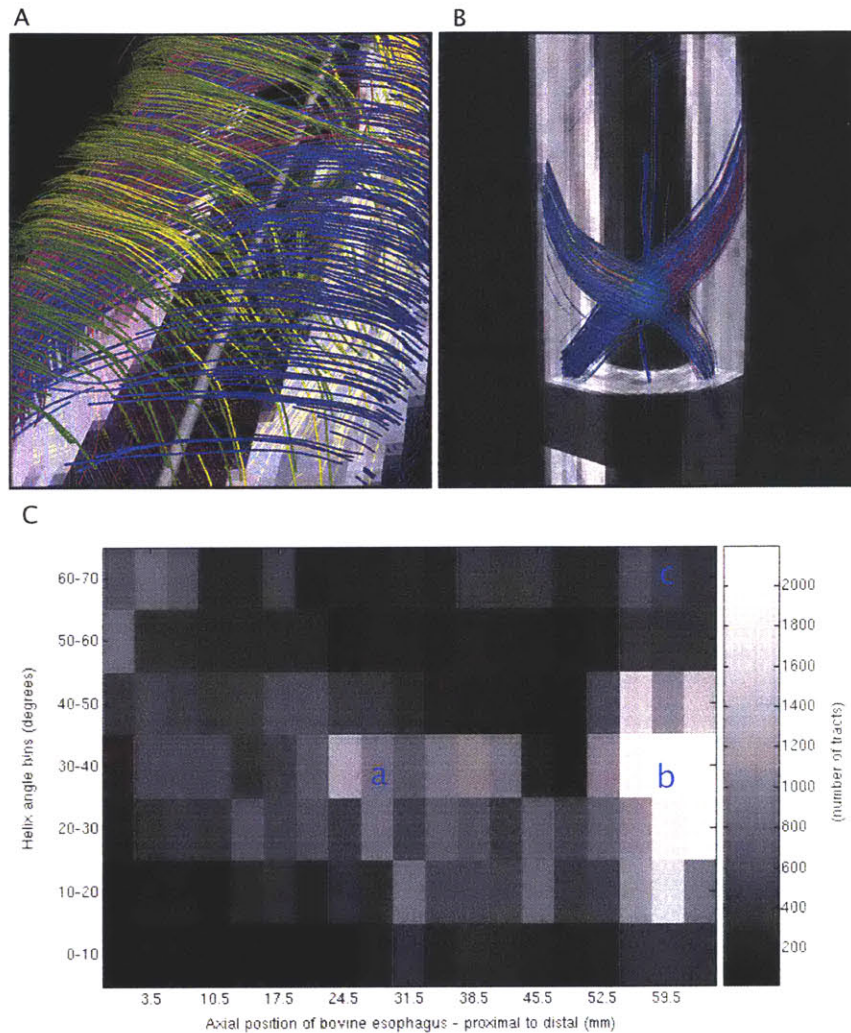
Figure 5.2.3: Demonstration of crossing helices in the proximal esophagus. (A) Displayed are the interwoven inner and outer layers at a zipper region observed along the length of the proximal esophagus. (B) Individual set of crossing myofibers demonstrating the presence of a cross planar relationship. (C) Histogram showing the distribution of helix angle as a function of position along the length of the esophagus, beginning in the proximal region and proceeding distally. The intensity of each bin is related to the number of tracts passing through an axially aligned region of interest and possessing the defined helix angle range. The image demonstrates a gradual reduction of helix angle from approximately 60° to 20° as a function of axial position (a). the high number of tracts in the region marked (b) is due to the slight tilt relative to the longitudinal axis exhibited by the dense circumferentially aligned tracts in the distal region. The appearance of high helix angle tracts in the distal esophagus (c) corresponds to the thin longitudinally aligned outer wall.
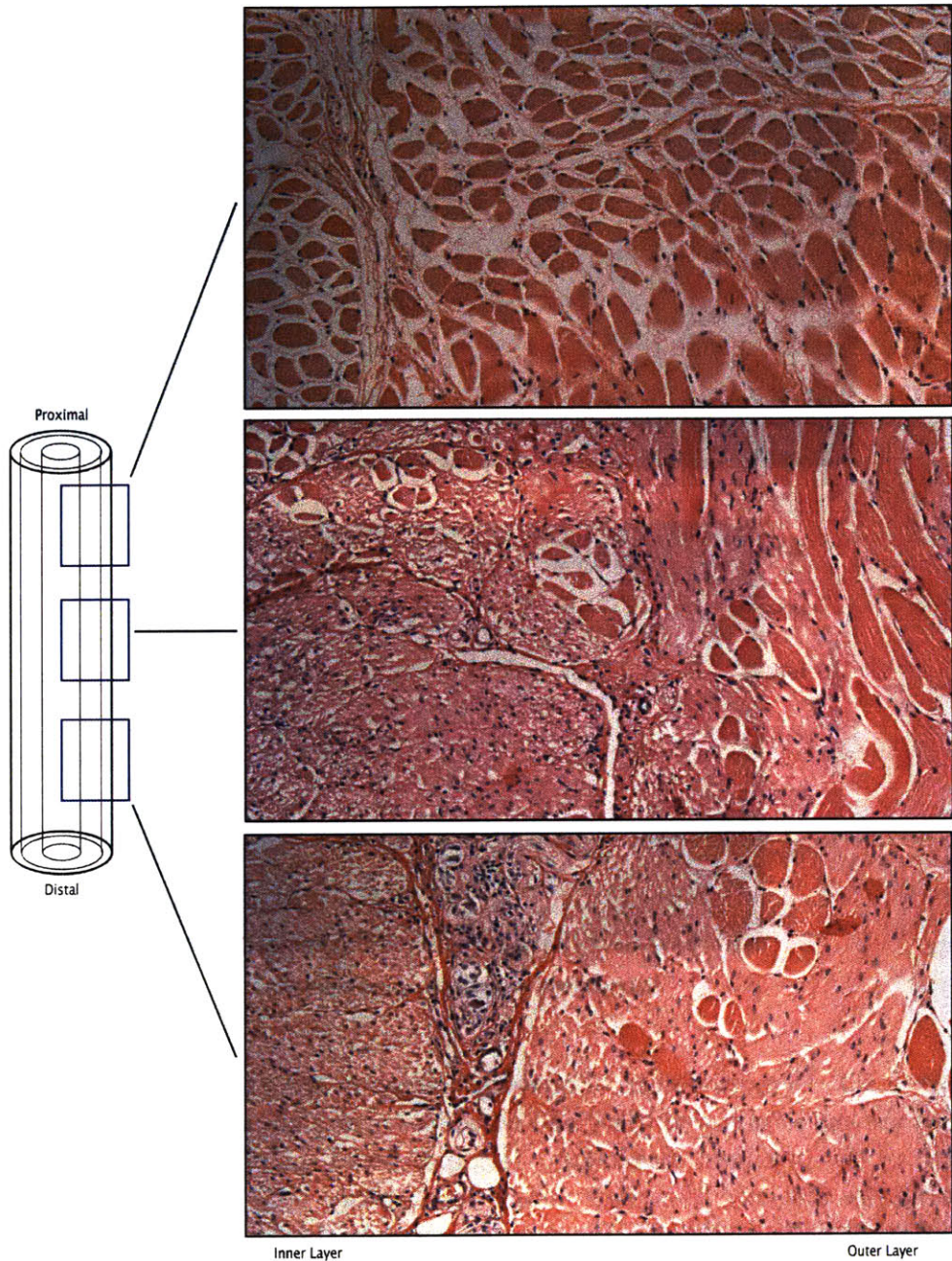
Figure 5.2.4: Histology of the esophageal muscularis. Circumferential sections. Skeletal muscle fiber bundles in the proximal esophagus principally perpendicular to the plane of the section. In the middle esophagus, we observe several populations of skeletal muscle fiber bundles, based on orientation, juxtaposed with relatively uniformly oriented smooth muscle regions. In the distal esophagus, more limited skeletal muscle bundles are observed perpendicular to the plane of the section relative to the predominant sheets of smooth muscle.

Proximal

Distal

Inner Layer – Low Magnification

High Magnification
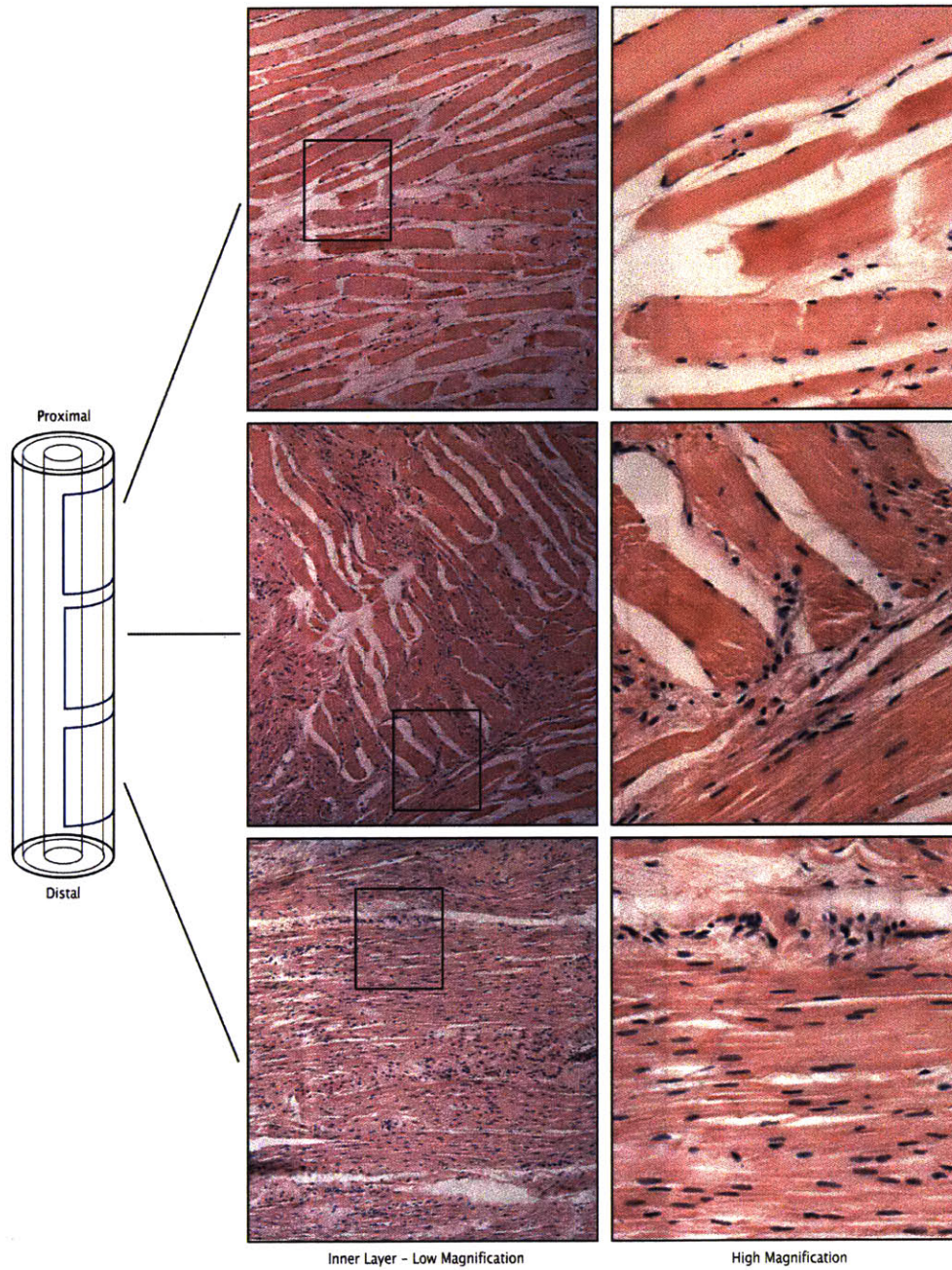
Figure 5.2.5: Histology of the esophageal muscularis. En face orientation. Depicted are the in plane relationships of the skeletal and smooth muscle cells. when the plane of reference is the circumferential layer (parallel to the mucosa) of the tissue. Most significantly. we observe the varying angular relationships exhibited by the skeletal and smooth muscle. as a function of location in the proximal. middle and distal esophagus.

81
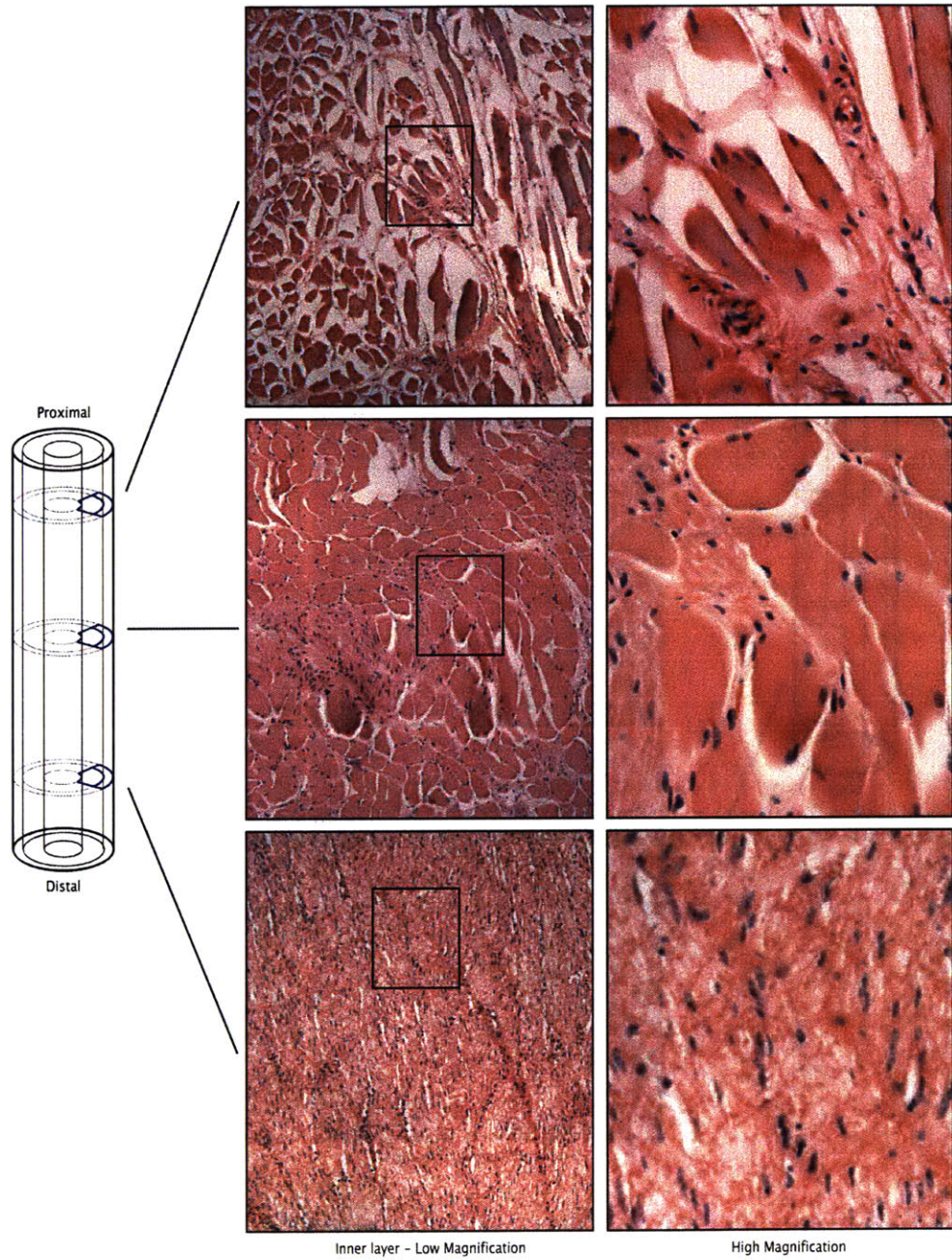
Figure 5.2.6: Histology of the esophageal muscularis. Axial orientation.

Chapter 6

Conclusion and Future Work

The purpose of this work was to explore various applications of diffusion weighted magnetic resonance imaging to studying the cytoarchitecture of complex muscles. In general there were two major technological directions pursued: (1) to apply diffusion imaging at the highest resolutions possible to understand how the diffusion function describes tissue microstructure, and (2) to image architecture in vivo and relate to active deformations.

6.1   Diffusion and aspects of microstructure

In the mouse tongue, we compared high resolution diffusion spectrum derived architecture with actual 3D microscopy data of the entire anterior tongue, and related dimensions of microstructure to the diffusion derived probability density function as well as provided a means to further validate DSI as reliable method of extracting fiber directions. Many questions remain; such as what are the precise biophysical barriers causing restricted diffusion, and what are the roles of diffusion time and diffusion gradient duration? Diffusion simulations should be expanded to incorporate permeable membranes and subcellular components to see whether these parameters can be used to explain the predicted PDF.

We performed initial data acquisition and preliminary analysis of the sheep heart for both normal and remodeled architecture. Further analysis of this data should be

performed to include modeling of the proposed unified toroidal helical structure to better understand why the normal heart, and perhaps even the infarcted heart, are shaped like they are. Another interesting application of diffusion spectrum imaging is the potential study of the effect of missing adhesion proteins in cardiac muscle mesocale architecture. Studies of muscle degeneration that have been performed using histological and electron microscopic analysis [44] may benefit from the ability to see larger scale trends in three dimensions. The results of such a study would likely even help us better understand normal cardiac myoarchitecture.

6.2 Diffusion imaging as a template for active deformation

In an effort to bring diffusion imaging of myoarchitecture closer to the clinical realm, we developed methods which allow derivation of the human tongue musculature in vivo. The validity of these fiber tracts as a template for contractility was explored through comparison to local strain rate during swallowing, derived with phase contrast MRI. The techniques were successful in capturing complex strain rate events in within the tongue, and appeared to identify activity in certain muscles, though it is unknown whether expansive and contractile events were a result of active compression of constituting muscle fibers, or were passive deformations resulting from activity external to the field of view. Opportunities for improvement exist in the MRI methods for imaging both architecture and mechanics.

Lingual muscle architecture was derived in vivo with diffusion tensor MRI, as opposed to high angular resolution methods, because it was the most robust in regards to motion artifact. However, DTI allows the extraction of only one diffusion maxima per voxel, which may not adequately describe local muscle architecture, especially in the tongue for which significant regions contain fibers oriented in two or three major directions. Therefore, methods which are able to resolve multiple fiber directions, such as DSI or q-ball should be implemented to improve the anatomical validity of

the orientation data. On the other hand, the current protocol takes around 5 minutes to complete a scan, which still seems too long for clinical use. With surface coils better optimized for the tongue, higher field magnets and slightly larger voxels, I am confident this value can be reduced. We are approaching the point of high enough quality data and fast enough scan times so that these methods may be used for image-guided surgery.

Local strain rates were derived in 2D with phase contrast MRI. Based on high inter-subject variation, but low intra-subject variation, we predict that strain rate acquisitions must be obtained with shorter temporal resolution than 100 ms in order to fully determine the mechanical function of the tongue during a swallow. Also, the acquisition of 3D strain rate using phase contrast would greatly add to its utility, but several issues need to be solved to make this feasible. An interesting alternative proposition to derive information about 3D deformation would be to acquire DTI tractography in two muscular poses and base the measure of deformation on the observed tract displacement.

The implications of the unique decreasing-helix-angle architecture discovered in the cow esophagus could be better understood through determination of the strain fiield using similar methods as those used in the tongue in vivo; or through finite element analysis. DW-MRI derived muscle architecture is well suited for direct insertion into finite element analysis because the data is in the form of a vector field. The capacity to generate finite element mesh directly from MRI image data is well known [28, 16]. The combination of diffusion derived fiber architecture with 3D mesh generation could result in a low preparation time for anatomically accurate models. These simulations could constitute the basis for testable mechanical hypotheses.

In conclusion, the diffusion weighted imaging methodology is very versatile and capable of deriving mechanically-relevant, complex muscle architecture. Ideally, the methods will be applied in progressively more clinical studies.

Appendix A

Diffusion weighted imaging specimen preparation

In general, the fabrication of a satisfactory mounting to device is critical to successful imaging of ex vivo specimens. The following are some recommended points to consider:

- select or construct a coil with a sensitive volume of the correct dimensions for the tissue sample being imaged.

- select or construct a non-magnetic container with exterior diameter that fits solidly within the coil with a total length at least *three times* that of the sensitive volume to avoid field distortion due to air/solid interfaces

- securely mount specimen in container to avoid motion artifact over the multiple hours of scanning, but also avoid physically deforming the specimen as much as possible

- consider specimen care prior to imaging: if fixation is necessary the specimens can still be successfully imaged, but our experience has been the best with fresh tissue soaked in 0.6 mM Gadolinium solution to reduce the signal relaxation time, thereby allowing more averages in same amount of time.

Bibliography

[1] H. Ashikaga, J.C. Criscione, J. H. Omens, J.H. Covell, and N.B. Ingels. Transmural left ventricular mechanics underlying torsional recoil during relaxation. *Am J Physiol Heart Circ Physiol*, 286:640–647, 2003.

[2] Eytan Bardan, Mark Kern, Ronald C Arndorfer, Candy Hofmann, and Reza Shaker. Effect of aging on bolus kinematics during the pharyngeal phase of swallowing. *Am J Physiol Gastrointest Liver Physiol*, 290(3):G458–G465, Mar 2006.

[3] P.J. Basser. Fiber-tractography via diffusion tensor MRI (DT-MRI). Presented at the 6th Annual Meeting of the International Society of Magnetic Resonance ISMRM, Sydney, Australia, 1998.

[4] P.J. Basser, J. Mattiello, and D. LeBihan. MR diffusion tensor spectroscopy and imaging. *Biophysical Journal*, 66:259–267, 1994.

[5] F. Bloch. Nuclear induction. *Physical review*, 70:460–474, 1946.

[6] P.T. Callaghan. *Principals of nuclear magnetic resonance microscopy*. Oxford Press, Great Britain, 1993.

[7] Gloria Chi-Fishman. Quantitative lingual, pharyngeal and laryngeal ultrasonography in swallowing research: a technical review. *Clin Linguist Phon*, 19(6-7):589–604, 2005.

[8] G.G. Cleveland, D.C. Chang, C.F. Hazelwood, and H.E. Rorschach. Nuclear magnetic resonance measurements of skeletal muscle: anisotropy of the diffusion coefficient of the intracellular water. *Biophys J*, 16:1043–1053, 1976.

[9] D.G. Cory and A.N. Garroway. Measurement of translational displacement probabilities by nmr: an indicator of compartmentation. *Magnetic Resonance Medicine*, 14:435–444, 1990.

[10] B.M. Damon, Z. Ding, A.W. Anderson, A.S. Freyer, and J.C. Gore. Validation of diffusion tensor MRI-based muscle fiber tracking. *Magnetic Resonance Medicine*, 48:97–104, 2002.

[11] N.E. Diamant. Neuromuscular mechanisms of primary peristalsis. *Am J Med*, 103(5A):40S–43S, 1997.

[12] J. Dou, T.G. Reese, W.Y.I. Tseng, and V. J. Wedeen. Cardiac diffusion MRI with-out motion effects. *Magnetic Resonance Medicine*, 48:105–114, 2002.

[13] Jiangang Dou, Wen-Yih I Tseng, Timothy G Reese, and Van J Wedeen. Combined diffusion and strain mri reveals structure and function of human myocardial laminar sheets in vivo. *Magnetic Resonance Medicine*, 50(1):107–113, Jul 2003.

[14] Y. Fan, H. Gregersen, and G.S. Kassab. A two-layered mechanical model of the rat esophagus. experiment and theory. *Biomed Eng Online*, 3(1):40, 2002.

[15] Samuel Makepeace Felton, Terry Alden Gaige, Timoth G. Reese, Van J. Wedeen, and Richard J. Gilbert. Mechanical basis for lingual deformation during the propulsive phase of swallowing as determined by phase contrast magnetic resonance imaging. *J Appl Physiol*, In Press, 2007.

[16] P. Frey and H. Borouchaki. Delaunay tetrahedralization using an advancing-front approach. In Proc. of 5th International Meshing Roundtable, 1996.

[17] Y.C. Fung. *Biomechanics: Mechanical Properties of Living Tissues*. Springer, New York (2nd Edition), 1993.

[18] T.A. Gaige, T. Benner, R. Wang, V.J. Wedeen, and R.J. Gilbert. Three dimensional myoarchitecture of the human tongue determined in vivo by high resolution diffusion tensor imaging with tractography. *J Magnetic Resonance Imaging*, In press, 2007.

[19] C.J. Galban, S. Maderwald, K. Uffman, A. deGrieff, and M.E. Ladd. Diffusive sensitivity to muscle architecture: a magnetic resonance diffusion tensor imaging study of the human calf. *Eur J Appl Physiol*. 93:253–262, 2004.

[20] L. Garrido, V.J. Wedeen, K.K. Kwong, U.M. Spencer, and H.L. Kantor. Anisotropy of water diffusion in the myocardium of the rat. *Circ Res*. 8:554 560, 1994.

[21] R. J. Gilbert, S. Daftary, T. A. Campbell, and R. M. Weisskoff. Patterns of lingual tissue deformation associated with bolus containment and propulsion during deglutition as determined by echo-planar mri. *J Magnetic Resonance Imaging*. 8(3):554–560, 1998.

[22] Richard J Gilbert, Lee H Magnusson, Vitaly J Napadow, Thomas Benner, Ruopeng Wang, and Van J Wedeen. Mapping complex myoarchitecture in the bovine tongue with diffusion-spectrum magnetic resonance imaging. *Biophys J*. 91(3):1014 1022, Aug 2006.

[23] Richard J Gilbert and Vitaly J Napadow. Three-dimensional muscular architecture of the human tongue determined in vivo with diffusion tensor magnetic resonance imaging. *Dysphagia*. 20(1):1–7, 2005.

[24] Richard J Gilbert, Van J Wedeen, Lee H Magnusson, Thomas Benner, Ruopeng Wang, George Dai, Vitaly J Napadow, and Kenneth K Roche. Three-dimensional myoarchitecture of the bovine tongue demonstrated by diffusion spectrum magnetic resonance imaging with tractography. *Anat Rec A Discov Mol Cell Evol Biol*. 288(11):1173 1182, Nov 2006.

[25] R.J. Gilbert, S. Daftary, G. Reese, R.M. Weisskoff, and V.J. Wedeen. Determination of lingual myoarchitecture in whole tissue by NMR imaging of anisotropic water diffusion. *American Journal of Physiology*, 75:363–369, 1998.

[26] R.J. Gilbert, L.H. Magnusson, V.J. Napadow, T. Benner, R. Wang, and V.J. Wedeen. Mapping complex myoarchitecture in the bovine tongue with diffusion spectrum magnetic resonance imaging. *Biophysical Journal*, 91:1014–1022, 2006.

[27] A.F. Gmitro and A.S. Alexander. Use of a projection reconstruction method to decrease motion sensitivity in diffusion weighed MRI. *Magnetic Resonance Medicine*, 29:835–838, 1993.

[28] E. Gradilin, S. Zachow, P. Deufihard, and H.C. Hege. Shape-based approach for the estimation of individual facial mimics in craniofacial surger planning. in proc, of SPIE meidcal imaging conference, San Diego, USA. 2002.

[29] H. Gray. *Anatomy of the Human Body, 20th Ed.* Online Version - http://www.bartleby.com/107/, 1918.

[30] J.V. Hajnal, M. Doran, A.S. Hall, A.G Collins, A. Oatridge, J.M. Pennock, I.R. Young, and G.M. Bydder. MR imaging of anisotropically restricted diffusion of water in the nervous system: technical, anatomic, and pathologic considerations. *J or Computer Assisted Tomography*, 15:1–18, 1991.

[31] A.A. Holmes, D.F. Scollan, and R.L. Winslow. Direct histological validation of diffusion tensor MRI in formaldehyde-fixed myocardium. *Magnetic Resonance Medicine*, 44:157–161, 2000.

[32] E.W. Hsu, D.L. Buckley, J.D. Bui, S.J. Blackband, and J.R. Forder. Two-component diffusion tensor MRI of isolated perfused hearts. *Magnetic Resonance Medicine*, 45:1039–1045, 2001.

[33] Lisa Jonasson. *Segmentation of diffusion weighted MRI using the level set framework*. PhD thesis, Ecole Polytechnique Federale de Lausanne, 2005.

[34] D.K. Jones. The effect of gradient sampling schemes on measure derived from diffusion tensor MRI: A Monte Carlo study. *Magnetic Resonance Medicine*, 51:807–815, 2004.

[35] P. J. Kahrilas, J. A. Logemann, S. Lin, and G. A. Ergun. Pharyngeal clearance during swallowing: a combined manometric and videofluoroscopic study. *Gastroenterology*, 103(1):128–136, Jul 1992.

[36] Kenton R. Kaufman, Kai-Nan An, and Edmund Y. S. Chao. Incorporation of muscle architecture into the muscle length-tension relationship. *Journal of Biomechanics*, 22(8-9):943–948, 1989.

[37] K.H. Kim, C. Buehler, and P.T.C. So. High-speed, two-photon scanning microscope. *Appl Opt*, 38:6004–6009, 1999.

[38] P.C. Lauterbur. No title. *Nature*, 242:190, 1973.

[39] D. LeBihan, J.F. Mangin, C. Poupon, C.A Clark, S. Pappata, N. Molko, and H. Chabriat. Diffusion testor imaging: concepts and applications. *J Magnetic Resonance Imaging*, 13:534–546, 2001.

[40] W.A. Lee, H. Huang, G. Feng, J.R. Sanes, E. N. Brown, P.T. So, and E. Nedivi. Dynamic remodelin of dendritic arbors in gabaergic interneurons of adult visual cortex. *Plos Biology*, 4(2):1–10, 2006.

[41] I.J. LeGrice, Y. Takayama, and J.W. Covell. Transverse shear along myocardial cleavage planes provides a mechanism for normal systolic wall thickening. *Circulation Research*, 77:182–193, 1995.

[42] C.P Lin, V.J. Wedeen, J.H. Chen, C. Yao, and W.Y. Tseng. Validation of diffusion spectrum magnetic resonance imaging with manganese-enhanced rat optic tracts and ex vivo phantoms. *Neuroimage*, 19(3):482–495, 2003.

[43] O. Mansfield and P.K. Grannel. No title. *Journal Phys*, C6:L422, 1973.

[44] DJ Milner, G Weitzer, D Tran, A Bradley, and Y Capetanaki. Disruption of muscle architecture and myocardial degeneration in mice lacking desmin. *J. Cell Biol.*, 134(5):1255–1270, 1996.

[45] P.P. Mitra and B.I. halperin. Effects of finite gradient-pulse widths in pulsed-field-gradient diffusion measurements. *Journal of Magnetic Resonance*, 113:94–101, 1995.

[46] S. Mori, B. Crain, V.P. Chacko, and P.C.M. van Zijl. Three dimensional tracking of axonal projections in the brain by magnetic resonance imaging. *Ann Neurol*, 45:265–269, 1999.

[47] M.E.J. Moseley, J. Kucharczyk, H.S. Asgari, and D. Norman. Anisotropy in diffusion-weighted MRI. *Magnetic Resonance Medicine*, 19:321–326, 1991.

[48] K.W. Moser and J.G. Georgiadis. Extraction and validation of correlation lengths from the interstitial velocity fields using diffusion-weighted MRI. *Magnetic Resonance Imaging*, 22(2):257–268, 2004.

[49] V. J. Napadow, Q. Chen, V. Mai, P. T. So, and R. J. Gilbert. Quantitative analysis of three-dimensional-resolved fiber architecture in heterogeneous skeletal muscle tissue using nmr and optical imaging methods. *Biophys J*, 80(6):2968–2975, Jun 2001.

[50] V. J. Napadow, Q. Chen, V. J. Wedeen, and R. J. Gilbert. Biomechanical basis for lingual muscular deformation during swallowing. *Am J Physiol*, 277(3 Pt 1):G695–G701, Sep 1999.

[51] M. A. Nicosia and J. A. Robbins. The fluid mechanics of bolus ejection from the oral cavity. *J Biomech*, 34(12):1537–1544, Dec 2001.

[52] M.A. Nicosia, J.G. Brasseur, J.B. Liu, and L.S. Miller. Local longitudinal muscle shortening of the human esophagus from high-frequency ultrasonography. *Am J Physiology Gastrointest Liver Physiol*, 281(4):G1022–1033, 2001.

[53] M.A. Nicosia, L.Y. Kossovich, and M.V. Wilde. A mathematical model of estimating muscle tension in vivo during esophageal bolus transport. *J Theoretical Biology*, 219(2):235–255, 2002.

[54] S. Ogata, K. Mine, Y. Tamatsu, and K. Shimada. Morphological study of the human chondroglossus muscle in Japanese. *Ann Anat*, 184:493–499, 2002.

[55] A. Pal and J.G. Brasseur. The mechanical advantage of local longitudinal shortening on peristaltic transport. *J Biomech Eng*, 124(1):94–100, 2002.

[56] N.G. Papadakis, D. Xing, C.L. Huang, L.D. Hall, and T.A. Carpenter. A comparative study of acquisition schemes for diffusion tensor imaging using MRI. *Journal of Magnetic Resonance*, 137:67–82, 1999.

[57] D. Paydarfar, R. J. Gilbert, C. S. Poppel, and P. F. Nassab. Respiratory phase resetting and airflow changes induced by swallowing in humans. *J Physiol*, 483 (Pt 1):273–288, Feb 1995.

[58] C. Pierpaoli, P. Jezzard, P.J. Basser, A. Barnett, and G. DiChiro. Diffusion tensor MR imaging of the human brain. *Radiology*, 201:637–648, 1996.

[59] E.M. Purcell, H.C. Torrey, and R.V. Pound. Resonance absorption by nuclear magnetic moments in a solid. *Physical Review*, 69:37, 1946.

[60] T.G. Reese, O. Heid, R.M. Weisskoff, and V.J. Wedeen. Reduction of eddy-current-induced distortion in diffusion MRI using a twice refocused spin-echo. *Magn Res Med*, 49:177–182, 2003.

[61] T.G. Reese, V.J. Wedeen, and R.M. Weisskoff. Measuring diffusion in the presence of strain. *Journal of Magnetic Resonance Series B*, 112:253–258, 1996.

[62] T.G. Reese, R.M. Weisskoff, R.N. Smith, B.R. Rosen, R.E. Dinsmore, and V.J. Wedeen. Imaging myocardial fiber architecture in vivo with magnetic resonance. *Magnetic Resonance Medicine*, 4:786–791, 1995.

[63] Timothy G Reese, David A Feinberg, Jiangang Dou, and Van J Wedeen. Phase contrast mri of myocardial 3d strain by encoding contiguous slices in a single shot. *Magnetic Resonance Medicine*, 47(4):665–676, Apr 2002.

[64] J. R. Reichenbach, R. Venkatesan, D. A. Yablonskiy, M. R. Thompson, S. Lai, and E. M. Haacke. Theory and application of static field inhomogeneity effects in gradient-echo imaging. *J Magnetic Resonance Imaging*, 7(2):266–279, 1997.

[65] Hiroshi Saito and Ichizoh Itoh. Three-dimensional architecture of the intrinsic tongue muscles, particularly the longitudinal muscle, by the chemical-maceration method. *Anotomical Science International*, 78:168–176, 2003.

[66] J.D. Schmahmann, D.N. Pandya, R. Wang, G. Dai, H.E. D'Arceuil, A.J. de Crespigny, and V.J. Wedeen. Association of fiber pathways of the brain: parallel observations from diffusion spectrum imaging and autoradiography. *Brain*, 130(3):630–653, 2007.

[67] U. Sinha and L. Yao. In vivo diffusion tensor imaging of human calf muscle. *J Magnetic Resonance Imaging*, 15:87–95, 2002.

[68] K. K. Smith. Morphology and function of the tongue and hyoid apparatus in varanus (varanidae, lacertilia). *J Morphol*, 187(3):261–287, Mar 1986.

[69] G. Steidle and F. Schick. Echoplanar diffusion tensor imaging of the lower leg musculature using eddy current nulled stimulated echo preparation. *Magnetic Resonance Medicine*, 55:541–548, 2006.

[70] E.O. Stejskal and J.E. Tanner. Spin diffusion measurements - spin echoes in presence of a time-dependent field gradient. *Journal of Chemical Physics*, 42:288–292, 1965.

[71] E.O. Stejskal and J.E. Tanner. Use of spin echoes in a pulsed magnetic field gradient to study anisotropic restricted diffusion and flow. *Journal of Chemical Physics*, 43:3597–3603, 1965.

[72] M. Stone, E.P. Davis, A.S. Douglas, M. NessAiver, R. Gullapalli, W.S. Levine, and A. Lundberg. Modeling the motion of the internal tongue from tagged cine-mri images. *J Acoust Soc Am.*, 109(6):2974–82, 2001.

[73] D.D. Streeter and D.L. Bassett. An engineering analysis of myocardial fiber orientation in pig's left ventrical in systole. *The Anatomical Record*, 155(4):503–511, 2005.

[74] T. Takeda, G. Kassab, J. Liu, J.L. Puckett, R.R. Mittal, and R. K. Mittal. A novel ultrasound technique to study the biomechanics of the human esophagus in vivo. *Am J Physiology, Gastrointestinal Liver Physiology*, 282(5):G785–793, 2002.

[75] F. Torrent-Guasp, M.J. Kocica, A.F. Corno, M. Komeda, F. Carreras-Costa, A. Flotats, J. Cosin-Aguillar, and H. Wen. Towards new understanding of the heart structure and function. *European Journal of Cardio-Thoracic Surgery*, 27:191–201, 2005.

[76] H. C. Torrey. Bloch equations with diffusion terms. *Phys. Rev.*, 104(3):563–565, Nov 1956.

[77] G. Toure and C. Vacher. Anatomic study of tongue architecture based on fetal histological sections. *Surg Radiol Anat*, 28:547–552, 2006.

[78] W.I. Tseng, Reese. T.G., R.M. Weisskoff, and V.J. Wedeen. Cardiac diffusion tensor MRI in vivo without strain correction. *Magnetic Resonance Medicine*, 42:393–403, 1999.

[79] David Solomon Tuch. *Diffusion MRI of Complex Tissue Structure*. PhD thesis, Massachusetts Institute of Technology, 2002.

[80] D.S. Tuch. Q-ball imaging. *Magnetic Resonance Medicine*, 52:1358–1372, 2004.

[81] D.S. Tuch, T.G. Reese, M.R. Weigel, N. Makris, J.W. Belleveau, and V.J. Wedeen. High angular resolution diffusion imaging reveals intravoxel white matter fiber heterogeneity. *Magnetic Resonance Medicine*, 48:577–582, 2002.

[82] C.C VanDonkelaar, L.J. Kretzers, P.H.M. Bovendeerd, L.M.A. Lataster, K. Nicolay, J.D. Janssen, and M.R. Drost. Diffusion tensor imaging in biomechanical studies of skeletal muscle function. *Journal of Anatomy*, 194:79–88, 1999.

[83] V. J. Wedeen, T. G. Reese, V. J. Napadow, and R. J. Gilbert. Demonstration of primary and secondary muscle fiber architecture of the bovine tongue by diffusion tensor magnetic resonance imaging. *Biophys J*, 80(2):1024–1028, Feb 2001.

[84] V. J. Wedeen, R. M. Weisskoff, T. G. Reese, G. M. Beache, B. P. Poncelet, B. R. Rosen, and R. E. Dinsmore. Motionless movies of myocardial strain-rates using stimulated echoes. *Magnetic Resonance Medicine*, 33(3):401–408, Mar 1995.

[85] V.J. Wedeen, T.G. Reese, D.S Tuch, M.R. Wiegell, J.G. Dou, R.M. Weissoff, and D. Chessler. Mapping fiber orientation spectra in cerebral white matter with Fourier-transform diffusion MRI. presented at the 8th Annual meeting of the International Society of Magnetic Resonance Medicine. Denver, Colorado. 2000.

[86] T. L. Wickiewicz, R. R. Roy, P. L. Powell, J. J. Perrine, and V. R. Edgerton. Muscle architecture and force-velocity relationships in humans. *J Appl Physiol*, 57(2):435–443, 1984.

[87] J.C. Wu, E.C. Wong, E.L. Arrindell, K.B. Simons, A. Jesmanowics, and J.S. Hyde. In vivo determination of the anisotropic diffusion of water and the T1 and T2 times in the rabbit lens by high-resolution magnetic resonance imaging. *Invest Opthalmol Vis Sci*, 34:2151–2158, 1993.

[88] J. Yang, D. Liao, J. Zhao, and H. Gregersen. Shear modulus of elasticity of the esophagus. *Ann Biomed Eng*, 32(9):1223–1230. 2004.

[89] Scott R Youmans and Julie A G Stierwalt. Measures of tongue function related to normal swallowing. *Dysphagia*. 21(2):102–111. Apr 2006.